On the road to metallic nanoparticles by rational design: bridging the gap between atomic-level theoretical modeling and reality by total scattering experiments†

Binay Prasai,[a] A. R. Wilson,[b] B. J. Wiley,[b] Y. Ren[c] and Valeri Petkov*[a]

The extent to which current theoretical modeling alone can reveal real-world metallic nanoparticles (NPs) at the atomic level was scrutinized and demonstrated to be insufficient and how it can be improved by using a pragmatic approach involving straightforward experiments is shown. In particular, 4 to 6 nm in size silica supported $Au_{100-x}Pd_x$ (x = 30, 46 and 58) explored for catalytic applications is characterized structurally by total scattering experiments including high-energy synchrotron X-ray diffraction (XRD) coupled to atomic pair distribution function (PDF) analysis. Atomic-level models for the NPs are built by molecular dynamics simulations based on the archetypal for current theoretical modeling Sutton–Chen (SC) method. Models are matched against independent experimental data and are demonstrated to be inaccurate unless their theoretical foundation, *i.e.* the SC method, is supplemented with basic yet crucial information on the length and strength of metal-to-metal bonds and, when necessary, structural disorder in the actual NPs studied. An atomic PDF-based approach for accessing such information and implementing it in theoretical modeling is put forward. For completeness, the approach is concisely demonstrated on 15 nm in size water-dispersed Au particles explored for bio-medical applications and 16 nm in size hexane-dispersed $Fe_{48}Pd_{52}$ particles explored for magnetic applications as well. It is argued that when "tuned up" against experiments relevant to metals and alloys confined to nanoscale dimensions, such as total scattering coupled to atomic PDF analysis, rather than by mere intuition and/or against data for the respective solids, atomic-level theoretical modeling can provide a sound understanding of the synthesis−structure−property relationships in real-world metallic NPs. Ultimately this can help advance nanoscience and technology a step closer to producing metallic NPs by rational design.

Introduction

With current science and technology moving rapidly to smaller scales, metallic nanoparticles (NPs) are being synthesized in increasing numbers and explored for various useful applications, ranging from catalysis[1,2] and magnetic storage media[3,4] to photonics[5,6] and drug delivery.[7,8] Advancing nanoscience and technology, however, face a major problem concerning transforming the current trial-and-fail approach to synthesize metallic NPs into synthesizing metallic NPs by rational design. This is not a trivial task since the outcome of

synthesis of any NPs, including metallic ones, depends on a number of hard-to-assess kinetic and thermodynamic factors. An important step toward solving the problem would be the development of new or streamlining of existing techniques for revealing accurately the outcome of synthesis of metallic NPs at the atomic level, that is, the atomic-level structure of the actual metallic NPs made.

Indeed several experimental techniques, such as total scattering involving high-energy synchrotron X-ray and/or neutron diffraction coupled to atomic Pair Distribution Function (PDF) analysis,[9–11] coherent diffraction,[12] High Resolution Transmission Electron Microscopy (HR-TEM),[13] Extended X-ray Absorption Fine Structure spectroscopy (EXAFS),[14] and others, have already proven very successful in revealing accurately the atomic-level structure of metallic NPs, wholly or in part. Experiments, however, can be costly and time demanding, especially when conducted on a large scale. A viable alternative for providing guidance on the synthesis and optimization of metallic NPs for practical applications is by inexpensive theore-

[a] Department of Physics, Central Michigan University, Mt. Pleasant, Michigan 48858, USA. E-mail: petko1vg@cmich.edu
[b] Department of Chemistry, Duke University, Durham, NC 27708, USA
[c] X-ray Science Division, Advanced Photon Source, Argonne National Laboratory, Argonne, Illinois 60439, USA
†Electronic supplementary information (ESI) available: XRD patterns, TEM and 3D structure modelling methodology. See DOI: 10.1039/c5nr04678e

tical modeling and prediction techniques such as, for example, Density Functional Theory (DFT), Molecular Dynamics (MD) and Monte Carlo (MC) simulations.[15–17] In particular, there has been a considerable amount of DFT work aimed at revealing the atomic and electronic structures of small size (~1 nm) metallic NPs as factors shaping their useful properties.[18,19] DFT, however, is virtually inapplicable to metallic particles larger than 1–2 nm in size which are of primary interest for practical applications. To circumvent DFT's limitations, less precise but more widely applicable approximations, such as the embedded atom method (EAM),[20,21] the Finnis–Sinclair (FS) method,[22] the glue method,[23] the Sutton–Chen (SC) method[24] and others, have been developed and used extensively. For the most part, these approximations have been tested and optimized against *ab initio* or experimental data for bulk metals and alloys possessing perfectly 3D periodic and long (μm)-range ordered atomic structures. However, more often than not, real-world metallic NPs are neither 3D periodic nor perfectly ordered at the atomic-scale. For example, atoms at the NP surface, which are about 30% of all atoms in 5 nm in size and spherical in shape metallic particles, have coordination spheres incomplete to various extents and, furthermore, experience significant relaxation/disorder due to factors such as increased NP surface tension[12] and/or an active NP environment.[25] In contrast, atoms deep inside metallic NPs are fully coordinated and typically much less affected by NP surface and environment effects. As a result, substantial NP segments, such as the NP surface and interior, are inherently quite dissimilar from a structural point of view. Furthermore, increasingly and deliberately, *e.g.* when in pursuit of a certain functionality, atoms throughout metallic NPs, and not only in particular NP segments, are being structured non-uniformly.[26,27] This opens the following questions: (i) is it possible for current theoretical modeling alone to reveal accurately real-world metallic NPs at the atomic level and, if not, (ii) how can the accuracy of theoretical modeling be improved to a level acceptable for practical applications? These questions appear legitimate considering the results of, among others, recent structure studies on Au–Pt NPs. In particular, while experiments have shown clearly that the ground-state structure of 5–7 nm in size Au–Pt particles synthesized and optimized with catalytic applications in mind is of random-alloy type,[28] theoretical modeling based on the EAM method[29] predicted that the ground-state structure of 5–7 nm in size Au–Pt particles should be of Pt core–Au shell type. Obviously, using EAM predictions as a structural basis for rationalizing the catalytic properties of the particular Au–Pt NPs studied would have hampered, if not completely derailed, efforts aimed at improving these properties.

Here we investigate the extent to which current theoretical modeling alone can reveal real-world metallic NPs at the atomic level in a more systematic way. In particular, we synthesized 4 to 6 nm in size Au core–Pd shell NPs and then optimized, *i.e.* activated, them for catalytic applications by a customary post-synthesis treatment involving heating under a reactive gas (O_2 & H_2) atmosphere. The treatment not only

removed organic agents capping the NP surface but also transformed the initially Au core–Pd shell NPs into Au–Pd alloy type ones. Note that, herein, NP size refers to NP diameter since all the NPs studied are largely spherical in shape. We built atomic-level models for both as-synthesized and post-synthesis treated Au–Pd NPs by Molecular Dynamics (MD) simulations based on the archetypal for metal and alloy atomic structure theory SC method. SC was chosen over other theoretical methods currently in use not only because it has been proven particularly successful[22,30] but also because it is relatively simple analytically, and assessing its parameters can be done in an unambiguous way. We also characterized the NPs structurally by total scattering experiments coupled to atomic PDF analysis. The theoretical models were matched against the independent experimental data and found to be in serious need for improvement. Accordingly, several parameters of the SC method were modified by a rigorous procedure so as to take into account information on the atomic ordering in actual metallic NPs studied. New models were built and validated both against the respective experimental atomic PDFs and in terms of energy, *i.e.* stability. The so-improved models were analyzed and their relevance to the actual Au–Pd NPs studied was ascertained, thus demonstrating a pragmatic approach to bridging the gap between current theoretical modeling of metallic NPs and reality. For completeness, the approach was also concisely demonstrated on 15 nm in size water-dispersed Au particles explored for bio-medical applications and 16 nm in size hexane-dispersed $Fe_{48}Pd_{52}$ particles explored for magnetic applications. Note that our study concentrated on $Au_{100-x}Pd_x$ alloy NPs (x = 30, 46 and 58) not only because of their importance in key technological reactions, such as the direct formation of hydrogen peroxide,[31] vinyl acetate synthesis,[32] carbon monoxide oxidation,[33] oxidation of primary alcohols,[34] and others, but also because of the lack of a clear understanding of the observed significant enhancement of their catalytic activity as compared to that of pure Au and Pd NPs.[35–39] The results presented here shed new light on the catalytic synergy of Au and Pd species in Au–Pd alloy NPs, helping highlight the usefulness of our approach for practical applications.

Experimental

Synthesis of NPs studied

Au–Pd NPs were synthesized by depositing shells of one, two and four Pd layers on pre-made 4 nm Au seeds as described in ref. 40. The resulting Au core–Pd shell NPs had an overall chemical composition of $Au_{70}Pd_{30}$, $Au_{54}Pd_{46}$ and $Au_{42}Pd_{58}$, respectively, as determined by inductively coupled plasma atomic emission spectroscopy (ICP-AES) experiments described below. As-synthesized Au core–Pd shell NPs were deposited on fine silica powder and then optimized, *i.e.* activated, for catalytic applications by a controlled treatment involving 1 hour of heating under an O_2 atmosphere at 700 K followed by 1 hour of heating under a H_2 atmosphere at the

same temperature. The treatment removed organic molecules capping the NP surface and transformed the initially Au core–Pd shell type NPs into Au–Pd alloy type ones. The transformation did not affect the overall chemical composition of Au–Pd NPs significantly as HAADF-STEM and ICP-AES experiments described below showed. Hence, herein the overall chemical composition of both as-synthesized and post-synthesis treated Au–Pd NPs is denoted by $Au_{100-x}Pd_x$ ($x = 30, 46$ and 58) NPs. However, to differentiate them clearly, the as-synthesized (Au core–Pd shell) and obtained from them Au–Pd alloy NPs are hereafter referred to as "fresh" and "fully activated" Au–Pd NPs, respectively. Note that, following common practices, both fresh and fully activated Au–Pd NPs were kept in small sealed glass vials and were transported in this manner to various instruments (*e.g.* TEM, synchrotron XRD *etc.*) used for their characterization. The NPs were briefly exposed to air when loaded into the respective instruments and then kept sealed throughout the measurements.

Au NPs were synthesized by the protocol fully described in ref. 41. The as-synthesized Au NPs were not treated further but kept in water as required by the targeted bio-medical applications, including bio-imaging and drug delivery.[42–44]

Fe–Pd NPs were synthesized by the protocol fully described in ref. 44. The as-synthesized alloy-type NPs were not treated further but kept in hexane to avoid any oxidation that would be detrimental to the targeted magnetic applications. Here we concentrate on the $Fe_{48}Pd_{52}$ alloy NPs because of their particular importance to magnetooptics and high-density magnetic recording.[45,46]

The water-dispersed Au and hexane-dispersed $Fe_{48}Pd_{52}$ NPs were also sealed in small glass vials and transported in this way to various instruments (*e.g.* TEM, synchrotron XRD *etc.*) used for their characterization. Drops of the solutions were directly loaded into the instruments and thus were never exposed to air during our studies.

Determination of the size, shape, and chemical composition of the NPs studied

The size and shape of the Au seeds, Au NPs, and the fresh (Au core–Pd shell type) and fully activated (alloy type) $Au_{100-x}Pd_x$ NPs ($x = 30, 46$ and 58) were determined by Transmission Electron Microscopy (TEM) using a JEM-2200FS microscope operated at 200 kV. Exemplary TEM and high-resolution (HR)-TEM images are shown in Fig. S1 and S2,† respectively. As can be seen in the figures, (i) the Au seeds and pure Au NPs are, respectively, 4.1(±0.6) and 15(±1.5) nm in size and are spherical in shape, (ii) the fresh (core–shell type) $Au_{100-x}Pd_x$ NPs also are spherical in shape and are approximately 4.5(±0.9), 5.0 (±0.9) and 5.5(±0.9) nm in size for $x = 30$ (one Pd layer), $x = 46$ (two Pd layers) and $x = 58$ (four Pd layers), respectively, and (iii) the fully activated $Au_{100-x}Pd_x$ alloy NPs ($x = 30, 46$ and 58) retain the spherical shape and size of the respective fresh ones. Note that the observed step-wise increase in the size of $Au_{100-x}Pd_x$ NPs ($x = 30, 46$ and 58) with Pd content, x, is to be expected since $x = 30, 46$ and 58 are NPs prepared by depositing shells of one, two and four Pd layers, respectively, onto Au

seeds of constant (~4.1 nm) size. In line with earlier studies,[45] data in Fig. S3† show that $Fe_{48}Pd_{52}$ alloy NPs are 16(±1.5) nm in size and spherical in shape.

Here it is worth mentioning that HR-TEM images indicated that all of the metallic NPs studied here exhibit good overall crystallinity and, as usual, some atomic positional (structural) disorder. The disorder is particularly enhanced for atoms close to the NP surface.

The overall chemical composition of the fresh and fully-activated $Au_{100-x}Pd_x$ NPs ($x = 30, 46, 58$) and $Fe_{48}Pd_{52}$ alloy NPs was determined by inductively coupled plasma atomic emission spectroscopy (ICP-AES) using a Perkin Elmer 2000 DV ICP-OES instrument. Samples were dissolved in aqua regia and then diluted to concentrations in the range of 1 to 50 ppm. Calibration curves were made from dissolved standards in the same acid matrix as the unknowns. Standards and unknowns were analyzed 5 times each, resulting in <3% error in the reported chemical composition. Within the error limits, no appreciable difference between the chemical composition of the fresh (core–shell) and respective fully activated (alloy-type) Au–Pd NPs was observed. A similar result, *i.e.* that the activation of Au–Pd NPs for catalytic applications by a thermo-chemical treatment conducted with due care does not necessarily induce significant changes in the overall NP chemical composition, size and shape, has been reported by Dash *et al.*[39]

The chemical ordering pattern of fresh and fully activated $Au_{100-x}Pd_x$ NPs ($x = 30, 46, 58$) and $Fe_{48}Pd_{52}$ NPs was determined by High-Angle Annular Dark-Field (HAADF) Scanning TEM (STEM) imaging. Experiments were done on a JEOL JEM 2100F instrument operated at 200 keV in STEM mode. The lens settings combined with the corrector tuning gave a spatial resolution of approximately 90 pm. Exemplary HAADF-STEM images of fresh and fully activated $Au_{100-x}Pd_x$ NPs ($x = 30, 46, 58$) are shown in Fig. S4.† The images confirm the pre-desired Au core–Pd shell chemical pattern of fresh Au–Pd NPs and the alloy-type character of post-synthesis treated ones. For completeness, HAADF-STEM images of $Au_{100-x}Pd_x$ ($x = 30, 46, 58$) NPs which were post-synthesis treated under an O_2 atmosphere alone are also shown in this figure. An exemplary HAADF-STEM image of $Fe_{48}Pd_{52}$ NPs is shown in Fig. S3.† In line with earlier studies,[45] data in the figure indicate that the $Fe_{48}Pd_{52}$ NPs studied here are of alloy type character.

X-ray photoelectron spectroscopy

X-ray Photoelectron Spectroscopy (XPS) measurements on fully activated silica supported $Au_{100-x}Pd_x$ NPs ($x = 30, 46$ and 58) were performed on a Physical Electronics Quantum 2000 scanning ESCA microprobe including a focused monochromatic Al K_α X-ray (1486.7 eV) source for excitation, a spherical section analyzer and a 16-element multichannel detection system. The percentages of individual metallic species in the NPs were determined by analyzing the areas of the respective XPS peaks. The relative ratio of metallic species in the NPs determined by XPS, which is mostly sensitive to the NP surface, was consistent with the overall NP composition determined by ICP-AES. The results indicated some but insignificant oxidation of the

NP surface most likely due to air exposure of the samples before the XPS measurements.

Total scattering experiments

All NPs studied here were subjected to high-energy synchrotron X-ray diffraction (XRD) experiments at room temperature. Experiments were carried out at the 11-ID-C beamline of the Advanced Photon Source at Argonne using X-rays with an energy of 115 keV (λ = 0.1080 Å). Diffraction data were collected up to wave vectors of 25 Å^{-1} allowing resolving of NP structural features closer than 0.01 Å. The experimental set-up was calibrated with a high-purity Si powder standard. A polycrystalline Au standard was also measured. During the measurement batches of fine silica powder supported Au seeds, fresh and fully activated Au$_{100-x}$Pd$_x$ (x = 30, 46, 58) NPs were sealed in 1.5 mm glass capillaries. An empty glass capillary and silica powder alone were also measured separately. Au NPs were measured as obtained and dispersed in water. Water alone contained in a glass capillary was measured as well. Fe$_{48}$Pd$_{52}$ NPs were measured as obtained and dispersed in hexane. Hexane alone contained in a glass capillary was also measured. Experimental synchrotron high-energy XRD patterns for Au seeds, fresh and fully activated Au$_{100-x}$Pd$_x$ (x = 30, 46, 58) NPs, as corrected for detector dead time, sample absorption, empty glass capillary, silica support and other background-type (air *etc.*) scattering, are shown in Fig. S5.† The experimental synchrotron high-energy XRD patterns for Au NPs, as corrected for detector dead time, sample absorption, empty glass capillary, water and other background-type (air *etc.*) scattering, are shown in Fig. 3 in ref. 41. The experimental synchrotron high-energy XRD patterns for Fe$_{48}$Pd$_{52}$ NPs, as corrected for detector dead time, sample absorption, empty glass capillary, hexane and other background-type (air *etc.*) scattering, are shown in Fig. 1 in ref. 46. As can be seen in the respective figures, all experimental synchrotron high-energy XRD patterns exhibit a few broad, strongly overlapping peaks at low diffraction (Bragg) angles and almost no distinct peaks at high diffraction angles, *i.e.* are rather diffuse in nature. This renders the well-established, sharp Bragg peak-based procedures for revealing the atomic-level structure of bulk metals and alloy inapplicable to metallic NPs. Therefore, we considered the diffuse XRD patterns in terms of so-called atomic PDFs $G(r)$ instead. The approach is advantageous[9–11,28] since, contrary to the respective diffuse XRD patterns, atomic PDFs show several distinct peaks allowing convenient testing and refinement of atomic-level models for metallic NPs. The derivation of experimental PDFs was performed according to well-established procedures.[47] Note that the experimental synchrotron high-energy XRD patterns and so the atomic PDFs derived from them reflect ensemble averaged structural features of all metallic NPs sampled by the synchrotron X-ray beam in the respective experiments in the way traditional powder XRD patterns reflect ensemble averaged structural features of all polycrystallites sampled by the X-ray beam in those experiments. Using NP ensemble averaged structural features to understand and explain NP ensemble averaged properties (*e.g.* catalytic,

magnetic, optical *etc.*) puts the NP synthesis–structure–property exploration on the same footing.

Results and discussion

First, we considered thoroughly silica supported Au–Pd NPs. As discussed above, revealing accurately the atomic-level structure of both as-synthesized and post-synthesis treated metallic NPs is of particular importance for advancing nanoscience and technology. For this reason, we considered both fresh and fully activated Au–Pd NPs. The atomic-level structure of Au–Pd NPs not fully optimized for catalytic applications, such as those treated under an O$_2$ atmosphere alone, was considered in much lesser detail. Experimental atomic PDFs $G(r)$ for fresh (core–shell), treated under an O$_2$ atmosphere alone and fully activated Au$_{100-x}$Pd$_x$ alloy NPs (x = 30, 46, 58), as derived from the respective XRD patterns of Fig. S5,† are summarized in Fig. 1. As can be seen in the figure, the experimental PDFs show a sequence of well-defined peaks. By definition, peaks in an atomic PDF for binary, *i.e.* A–B type, NPs should reflect three chemically distinct pairs of atoms, *i.e.* A–A, A–B and B–B pairs of atoms, immediate and all farther neighbors, within the NPs studied. Accordingly, peaks in the experimental PDFs of Fig. 1 reflect all Au–Au, Au–Pd and Pd–Pd pairs of atoms in the Au–Pd NPs studied here. Note that since atoms close to or at opposite sides of the NPs are separated the most, atomic PDFs of Fig. 1 may be expected to show distinct peaks up to distances close to the average size (diameter) of the respective NPs. As can be seen in Fig. 1, however, peaks in the experimental PDFs decay to zero at distances (~3.5 nm) shorter than the physical size of the respective Au–Pd NPs, which is ~4.5 to 5.5 nm as determined by TEM. The observed fast decay of the experimental PDFs indicates that atoms in the Au–Pd NPs studied here, especially those near the NP surface, suffer substantial positional disorder. Atomic positional disorder is common to metallic NPs due to finite NP size and NP environment effects.[9,10,13,14] The magnitude of this disorder in different systems of metallic NPs, however, can be substantially different due to details of the particular NP synthesis and post-synthesis treatment protocols employed.[48]

Experimental atomic PDFs for fresh and fully activated Au$_{100-x}$Pd$_x$ NPs (x = 30, 46 and 58) are compared in Fig. 2. As can be seen in the figure, peaks in the atomic PDFs for the fresh (core–shell) and fully activated (alloy-type) NPs differ in positions and intensities substantially. The difference reflects (i) the different distribution of Au and Pd species in the respective NPs (see the HAADF-STEM images in Fig. S3†) and (ii) the fact that Au and Pd atoms in Au–Pd NPs interact more strongly when intermixed together, as in the fully activated Au–Pd NPs, as compared to the case when they are largely kept apart, as in the fresh (Au core–Pd shell) NPs. Data in Fig. 2 also show that experimental atomic PDFs obtained by total scattering experiments are sensitive enough to differentiate between core–shell and alloy-type Pd–Au NPs and so can be
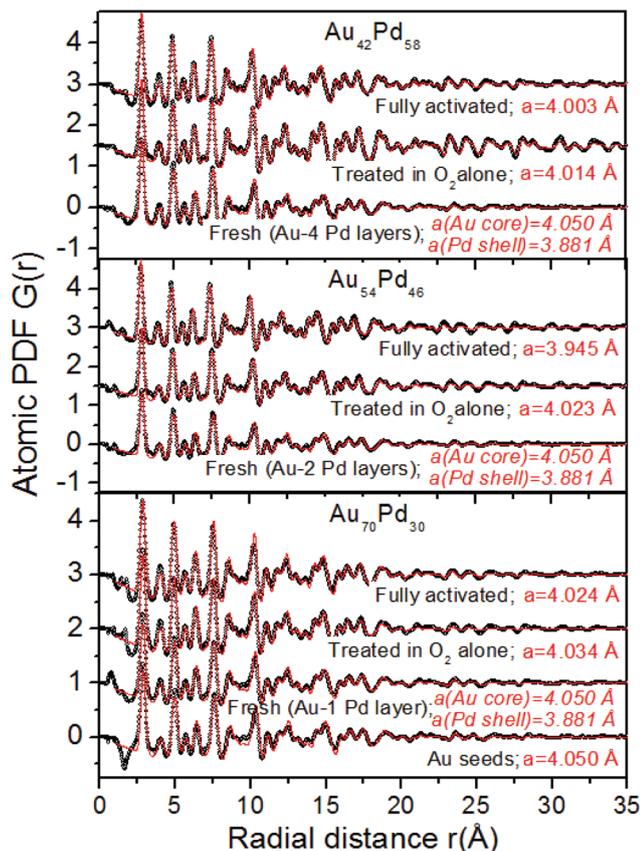
Fig. 1 Experimental (black symbols) and model (red lines) PDFs for Au seeds, fresh, post-synthesis treated under an O_2 atmosphere alone and fully activated (*i.e.* post-synthesis treated under an O_2 + H_2 atmosphere) $Au_{100-x}Pd_x$ NPs (x = 30, 46 and 58). The models feature perfectly 3D periodic, infinite fcc-type lattices. As discussed in the text, models for post-synthesis treated $Au_{100-x}Pd_x$ (alloy-type) NPs involve a single fcc lattice. On the other hand, models for fresh (core–shell type) NPs involve two independent fcc lattices: one for the Au core and one for the Pd shell. Values of the NP "fcc-lattice parameter", a, derived by adjusting the model fcc-lattices against the respective experimental PDFs are given by each data set. Goodness-of-fit indicators, R_{wp}, explained in the ESI,† for all model PDFs shown in the figure are in the range of 20–23%.

used to differentiate between competing models for their atomic-level structure.

Atomic-level models for fresh and fully activated $Au_{100-x}Pd_x$ NPs (x = 30, 46 and 58) were built by the SC method. In brief, the method treats atomic pair interactions in metals and alloys as the sum of two constituents. One accounts for the repulsion between metal atom cores and the other for the attractive force between metal atom cores due to the electrons surrounding them.[22,24]

Accordingly, the energy of atomic-level models, U, appears as a sum of an atomic pair potential $V(r_{ij})$ term and a local electron density (ρ_i) term defined as follows:

$$U = \sum_i \left[\sum_{j \neq i} \frac{1}{2} \varepsilon_{ij} V(r_{ij}) - c_i \varepsilon_{ij} (\rho_i)^{1/2} \right] \quad (1)$$
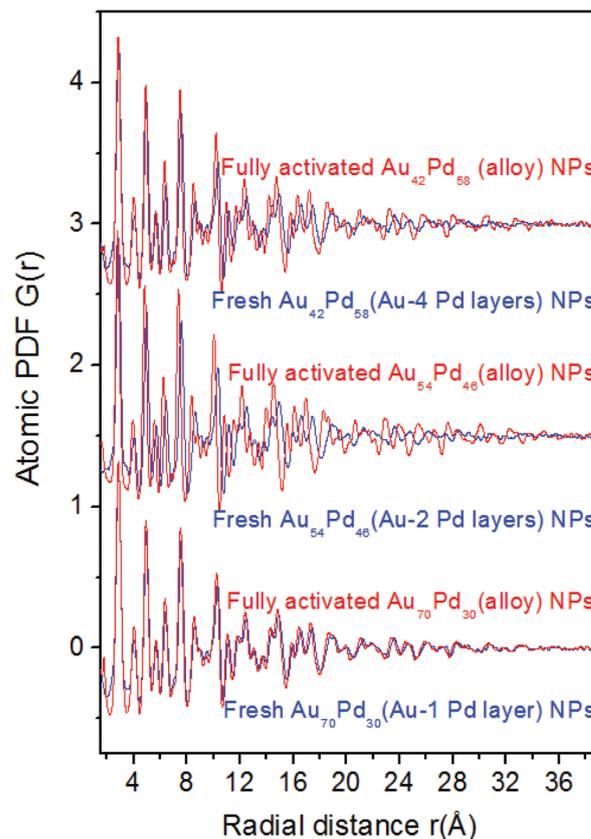
Fig. 2 Experimental atomic PDFs for fresh (blue lines) and respective fully activated (red lines) $Au_{100-x}Pd_x$ NPs (x = 30, 46 and 58). Note: fresh and respective fully activated NPs are virtually of the same overall chemical composition, size and shape even though the former are of Au core–Pd shell type and the latter are of Au–Pd alloy type (see the Experimental section). Peaks in the atomic PDFs for fresh and respective fully activated NPs differ in positions and intensities substantially. The difference reflects (i) the very different distribution of Au and Pd species in the fresh and respective fully activated NPs and (ii) the fact that, as explained in the text, atomic pair distances in the fresh and respective fully activated NPs are different due to the much stronger interactions between Au and Pd species in the latter relative to the former. Note: as also discussed in the text, the strength of interactions between Au and Pd species in fully activated NPs and, hence, the atomic pair distances in these NPs vary irregularly with the NP bimetallic composition. Accordingly, the level of dissimilarity between the atomic PDFs of fresh and respective fully activated NPs also varies irregularly with the NP bimetallic composition.

where

$$V(r_{ij}) = \left(\frac{a_{ij}}{r_{ij}} \right)^{n_{ij}} \text{ and } \rho_i = \sum_{j \neq i} \left(\frac{a_{ij}}{r_{ij}} \right)^{m_{ij}}. \quad (2)$$

The so-called "energy" parameter ε_{ij} (meV) and the dimensionless parameter c_i are used to appropriately scale the interatomic repulsive $V(r_{ij})$ and attractive (ρ_i) interactions, respectively. Parameters m_{ii} and n_{ii} are positive integers such that $n_{ii} > m_{ii}$. The parameter a_{ij} is a quantity used to appropriately scale distances r_{ij} between i and j type atoms in the struc-

Table 1 Currently used SC parameters for Au and Pd. Sizes[a] of Au and Pd atoms given in the table reflect the respective a_{ii} parameters

Metal	m_{ii}	n_{ii}	ε_{ii} (meV)	a_{ii} (Å)	c_i	Size$_{ij}$ (Å)
Au	8	11	7.8052	4.080	53.581	2.88
Pd	6	12	3.2864	3.891	148.205	2.75

[a] Atomic size = the respective SC parameter $a_{ij}/\sqrt{2}$.

ture models, including the shortest ones. The latter are nothing but the size (diameter) of i and j type atoms. The SC parameters currently used for Au and Pd, as taken from literature sources,[22,24,49] are given in Table 1. The parameters have been optimized against data for bulk Au and Pd metals. In particular, SC parameters a_{ii} for Au and Pd (the 5th column in Table 1) are the experimentally determined values of the fcc-lattice parameters of bulk Au and Pd. Accordingly, the Au and Pd atoms in the structure models based on SC, as applied currently, appear with the size of Au and Pd atoms (the 7th column in the table for convenience) in bulk Au and Pd, respectively.[50]

Typically, theoretical methods for modeling metallic alloys derive the interactions between unlike atoms, *i.e.* i–j type atomic interactions, as the average of the interactions between like atoms. At present, the SC method derives the strength of interactions between unlike atoms, in particular the energy parameter ε_{ij}, as a geometric average of the respective ε_{ii} and ε_{jj} parameters.[30] The SC parameter a_{ij}, used to scale distances between unlike atoms, is also derived as a geometric average of the respective a_{ii} and a_{jj} parameters. On the other hand, SC parameters m_{ij} and n_{ij} are derived as an arithmetic average of the respective m_{ii} and n_{jj} parameters as shown in eqn (3):

$$\varepsilon_{ij} = \sqrt{\varepsilon_{ii}\varepsilon_{jj}}, \quad a_{ij} = \sqrt{a_{ii}a_{jj}},$$
$$m_{ij} = \frac{m_{ii} + m_{jj}}{2} \text{ and } n_{ij} = \frac{n_{ii} + n_{jj}}{2}. \tag{3}$$

To be as realistic as possible we built SC based models for the fresh and fully activated Au–Pd NPs so as to reflect the size (4.5–5.5 nm; see Fig. S1 and S2†), shape (spherical; see Fig. S1 and S2†), overall chemical composition (see Table S1†) and chemical pattern (core–shell for fresh and an alloy-type for fully activated NPs; see Fig. S4†) of the actual Au–Pd NPs studied here. Au seeds were also modelled. For consistency, initial model configurations featured pieces of fcc lattices with lattice parameters corresponding to the SC parameters a_{ii} of Table 1. The configurations were optimized in terms of energy through Molecular Dynamics (MD) simulations using the parameters in Table 1 for Au–Au and Pd–Pd interactions/distances and using eqn (3) for deriving the interactions/distances between Au and Pd atoms. Details of the MD simulations are given in the ESI.† The models built in this way appeared to be similar to the models shown in Fig. S8† (for fresh NPs) and Fig. 6, left (for fully activated NPs), introduced later on. The models, however, produced atomic PDFs markedly inconsistent with the experimental ones in terms of peak positions, intensities and sharpness, as exemplified in Fig. 3. These
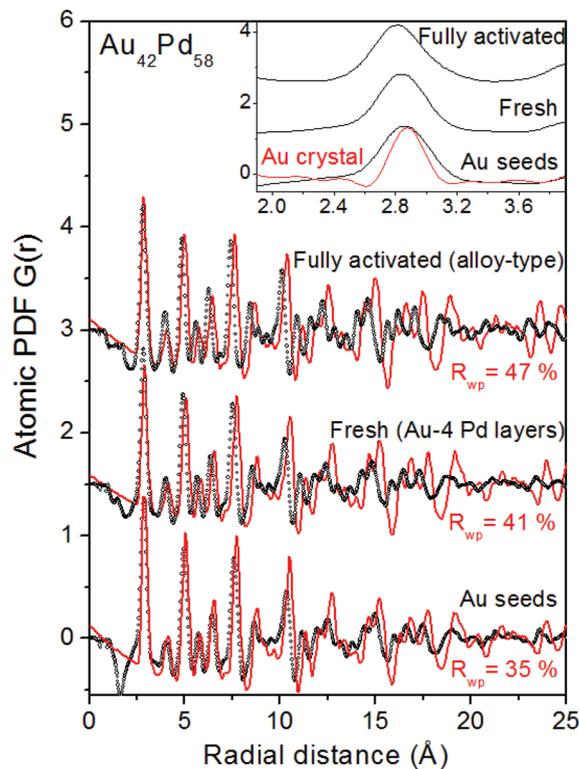
Fig. 3 Experimental (black symbols) and computed (red lines) atomic PDFs for Au seeds, fresh (Au core–4 Pd layer thick shell) and respective fully activated (alloy-type) $Au_{42}Pd_{58}$ NPs. Computed PDFs were derived from structural models built by MD simulations based on the SC method as applied currently. Peaks in the experimental and SC model-derived PDFs disagree in position, intensity and sharpness considerably (also see the respective R_{wp} values). The first peak in the experimental PDF for the Au seeds, fresh and fully activated $Au_{42}Pd_{58}$ NPs (black symbols) is shown in the inset. It appears rather broad, indicating the presence of strong atomic positional disorder in the Au seeds and the $Au_{42}Pd_{58}$ NPs. The disorder is made evident and then the first peak in the experimental PDF for the Au seeds is compared to that in the experimental PDF for polycrystalline (μ-sized crystallites) Au (red symbols). The former is much broader than the latter, revealing the presence of a higher degree of atomic positional disorder in metallic NPs in general, and in Au seeds and $Au_{42}Pd_{58}$ NPs studied here in particular. Furthermore, the former is shifted to lower r-values (2.86 Å) as compared to the latter (2.88 Å) indicating that the Au–Au metal bond length in Au seeds is shorter than that in bulk Au.

results showed clearly that the SC method cannot reveal accurately the atomic-level structure, and in particular the atomic pair distances, respective atomic pair numbers and strong atomic positional disorder, of either the as-synthesized or post-synthesis treated $Au_{100-x}Pd_x$ NPs ($x = 30$, 46 and 58) studied here.

To clarify the origin of the SC inaccuracy, we approached the experimental atomic PDFs with simplistic models constrained to an fcc-type crystal structure wherein atoms occupy identical sites in a perfectly 3D periodic, infinite fcc-type lattice. Such models made sense since bulk Au and Pd metals as well as bulk Au–Pd alloys are all fcc-type crystals.[50] Models for post-synthesis treated (alloy-type) Au–Pd NPs involved a single fcc lattice. Models for fresh Au–Pd NPs had to involve

two independent fcc-lattices: one for the Au core and another one for the Pd shell. Without including both lattices the model-derived atomic PDFs for the fresh Au–Pd NPs would not reproduce the experimental ones in good detail. This observation indicated that the Au cores and the Pd shells of the fresh Au–Pd NPs studied here are largely uncorrelated from a structural point of view. Similarly, uncorrelated cores and shells have also been observed within Pt core–Pd shell NPs.[51] The δ-function-like peaks in the atomic PDFs derived from the models were broadened by convolution with Gaussian functions so as to mimic the typically substantial structural disorder in metallic NPs (see the inset in Fig. 3). At the same time the PDFs were multiplied by an artificial, rapidly decaying with real space distance function to mimic the finite size of $Au_{100-x}Pd_x$ NPs (x = 30, 46 and 58) studied here. Finally, the unit cell parameters of the model fcc-lattices were refined such that model-derived atomic PDFs approached the corresponding experimental ones as closely as possible. Here it may be noted that the "lattice parameters" of metallic NPs are not as well defined as a physical quantity as those for their bulk counterparts. The reason is that the phrase "lattice parameters" implies the presence of a perfectly 3D periodic, infinite lattice while real-world metallic NPs are finite and not necessarily 3D periodic at the atomic level. Nevertheless, PDF data-derived "lattice parameters" of metallic NPs are useful merely because they reflect the set of interatomic distances, including metal-to-metal bond lengths, characteristic of the actual NPs under study and so may be used as a trustworthy "global indicator" of those distances. Computations were done with the help of the program PDFgui.[52] The results from the computations are shown in Fig. 1.

The results of empirical modeling showed that models featuring a fcc-type crystal structure reproduce all of the experimental PDFs in Fig. 1 in good detail indicating that atoms in both fresh and fully activated $Au_{100-x}Pd_x$ NPs (x = 30, 46 and 58) are arranged in an fcc-like manner. Noteworthy is also the fact that no structure models featuring other types of atomic ordering, including Au & Pd metal oxides, Au & Pd metal hydrides, or any others, had to be invoked for achieving the more than satisfactory level of agreement between the experimental and computed data in Fig. 1. Since the sensitivity of XRD to structurally and/or chemically distinct minor phases in materials is in the range of a few vol%, if not higher,[53] and furthermore, experimental atomic PDFs have proven sensitive to the presence of organic species adsorbed at the surface of metallic NPs,[54,55] it may be concluded that the Au–Pd NPs studied here were neither polluted with organic residues nor oxidized/hydrided significantly, if at all. Complementary XPS studies on the fully activated Au–Pd NPs indicated the same (see the Experimental section).

Inspection of the data in Fig. 1 also showed that the PDF-derived "fcc-lattice parameters", a, of Au seeds/cores (a = 4.050 Å) and Pd shells (a = 3.881 Å) are shorter by 0.7% and 0.4% as compared to those in bulk Au (a = 4.080 Å) and Pd (a = 3.891 Å) metals, respectively. This result is in line with the observed shift in position of the first peak in the experimental

PDF for Au seeds to lower-r values as compared to that of the first peak in the experimental PDF for bulk Au (see the inset in Fig. 3). Shortening/compression of the interatomic distances in metallic (*e.g.* Au) NPs up to 50 nm in size, including shortening/compression of the respective metal-to-metal bond lengths, has been very well documented and shown to arise mostly from NP finite size effects.[56] Yet, currently, finite NP size induced changes in metal-to-metal bond lengths in metallic NPs are largely not accounted for in the theoretical modeling of metallic NPs.

Furthermore, data in Fig. 1 show that the characteristic interatomic distances in fully activated $Au_{100-x}Pd_x$ alloy NPs (x = 30, 46 and 58), as reflected by their "fcc-lattice parameters", are rather different from those in the respective fresh and O_2 atmosphere treated alone Au–Pd NPs. Comparison with literature data shows that the characteristic interatomic distances in fully activated alloy $Au_{100-x}Pd_x$ alloy NPs (x = 30, 46 and 58) are also very different from those in bulk Au–Pd alloys.[39,49,50] The significance of the observed difference is best appreciated when PDF-derived "fcc-lattice parameters" for fully activated alloy Au–Pd NPs are depicted together with those for O_2 atmosphere treated alone Au–Pd NPs and bulk Au–Pd alloys,[49,50] as done in Fig. 4A. As can be seen in the figure, the characteristic interatomic distances in Au–Pd NPs treated under an O_2 atmosphere alone are longer by about 1.5% for NPs with the Au : Pd ratio of 50 : 50 and those in fully activated alloy Au–Pd NPs are shorter by about 2% for NPs with the Au : Pd ratio of 50 : 50 than the characteristic interatomic distances in bulk Au–Pd alloys of the same chemical composition. Metal-to-metal bond elongation of up to 3% in monometallic and a large number of binary and ternary metallic alloy NPs after treating under an O_2 atmosphere has been found by recent total scattering experiments and shortening/compression of up to 4% upon a subsequent post-synthesis treatment under a H_2 atmosphere has been documented by recent total scattering experiments.[25,57–61] Yet, current theoretical modeling of metallic NPs by and large does not account for details of the preparation of metallic NPs such as, for example, a post-synthesis thermal treatment under a reactive gas atmosphere.

Additionally, it is worth noting that contrary to the case of bulk Au–Pd alloys, the characteristic interatomic distances in fully activated Au–Pd alloy NPs, as reflected by their "lattice parameters", evolve very irregularly with the relative Au : Pd ratio (see Fig. 1 and 4A). An irregular evolution of the characteristic interatomic distances in binary (A–B) alloy NPs with the NP bimetallic composition has also been observed with Au–Cu alloy NPs.[62] Charge transfer between unlike metallic species combined with the natural optimization of atomic-level stresses are thought to cause this composition-dependent diversity in metal-to-metal atom bond lengths. Both of these processes are likely to play a role in the fully activated Au–Pd alloy NPs studied here since both the electronegativity[63] of 2.54 for Au and 2.2 for Pd and the elemental atomic size[59] of Au (2.88 Å) and Pd (2.75 Å) atoms are substantially dissimilar.[39,64,65] According to Pauling's theory of chemical bonding,[66–68] charge transfer between metallic species in
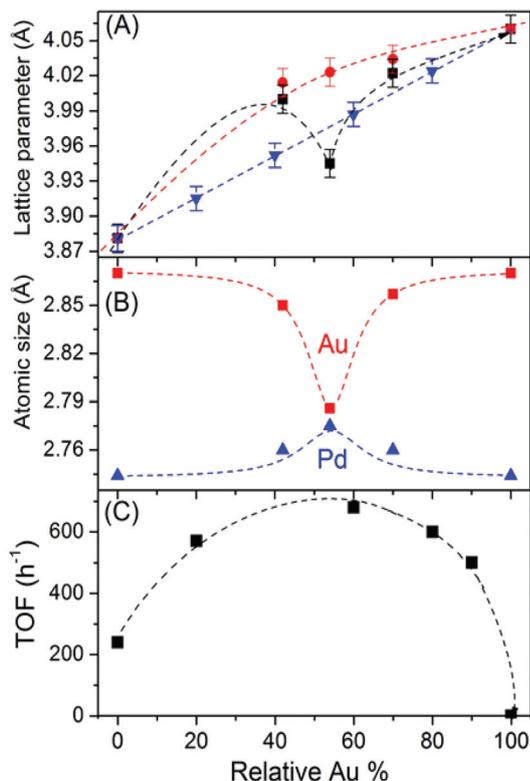
Fig. 4 (A) Atomic PDF-derived "lattice parameters" of the treated under an O_2 atmosphere alone (red circles) and fully activated (black squares) $Au_{100-x}Pd_x$ alloy NPs (x = 30, 46 and 58). Lattice parameters of bulk Au–Pd alloys obtained by traditional powder XRD[49,50] are also shown (down triangles in blue). Note: the "lattice parameters" of Au–Pd NPs evolve rather irregularly with the NP composition. On the other hand, the lattice parameters of bulk Au–Pd alloys evolve linearly with the alloy's composition obeying the so-called Vegard's law.[71] (B) Size of Au (red squares) and Pd (up triangles in blue) atoms that should be used by the SC method in modeling the atomic-level structure of fully activated $Au_{100-x}Pd_x$ alloy NPs (x = 30, 46 and 58) studied here. The size is adjusted against atomic PDFs obtained by total scattering experiments (see the text). (C) Evolution of the catalytic activity of Au–Pd alloy NPs, given in terms of turnover frequency (TOF), for the 2-octen-1-ol oxidation reaction with the NP composition.[7] Broken lines in (A), (B) and (C) are least-squares fits to the respective data points.

alloys may lead to a change in the size of species involved in that transfer. Furthermore, as suggested by Pearson[69] and confirmed by numerous experiments,[70] optimization of atomic-level stresses in binary alloys may involve "compression" of the larger and "expansion" of the smaller in size species so that the ratio of their sizes becomes as close to one as possible. This would lead to a decrease in the size of Au and an increase in the size of Pd species in the fully activated Au–Pd NPs. Undoubtedly, charge transfer and optimization of atomic-level stresses may considerably alter the sizes of constituent Au and Pd atoms and, hence, all of the atomic pair distances in fully activated Au–Pd NPs. If that were to happen the effect would be greatest when the Au : Pd ratio is about 50 : 50, i.e. when each metallic species would have the maximum possible number of unlike neighbors to interact/exchange charge with.

Indeed this is exactly what experimental data in Fig. 4A show. Yet, currently, theoretical modeling largely neglects the fact that metallic species, in particular Au and Pd ones (see Table 1), may change in size when alloyed at the nanoscale and tend to assume that the "lattice parameter" of alloy NPs changes linearly with the NP composition, i.e. strictly obeys the so-called Vegard's law (see Fig. 4A).[71] Evidently, the parameters of the SC method needed to be "tuned up" so that the combined effects of NP finite size, NP surface tension, details of the NP synthesis and post-synthesis treatment, such as the temperature and duration of the latter, and the inter-related charge transfer and change in metal-to-metal bond lengths[55,66–70] are all properly accounted for in modeling the $Au_{100-x}Pd_x$ NPs (x = 30, 46 and 58) studied here.

For this purpose, the currently used SC parameters were tuned up so that (i) the SC model-derived and respective PDF data-derived "global indicators" of the characteristic inter-atomic distances in $Au_{100-x}Pd_x$ NPs, i.e. the NP "lattice parameters", match each other, (ii) the SC model-derived atomic PDFs reproduce the full profile of the respective experimental ones in fine detail and (iii) the energy of SC models is minimized as much as possible. Achieving (i) to (iii) necessitated modifying the current SC procedure (see eqn (3)) for deriving the strength of interactions and bonding distances between the unlike atoms, i.e. the strength of interactions and bonding distances between Au and Pd atoms. This came as no surprise since the strength of interactions and bonding distances between unlike atoms keep their charge and size intact, as is the case with Au and Pd atoms in bulk Au–Pd alloys (see the strictly linear evolution of the lattice parameter of bulk Au–Pd alloys with the relative Au : Pd ratio shown in Fig. 4A), and those between unlike atoms exchanging charge and changing in size, as appears to be the case with Au and Pd atoms in the Au–Pd alloy NPs (see the non-linear evolution of the PDF-derived "lattice parameter" of Au–Pd alloy NPs with the relative Au : Pd ratio shown in Fig. 4A), may not be the same. The modification was done as follows: first, Au–Au and Pd–Pd atomic pair distances in the initial atomic configurations used in the MD simulations of Au–Pd NPs, i.e. the SC parameters a_{ii} for Au and Pd atoms shown in Table 1, were "re-scaled" so that the peaks in the MD model-derived PDFs come as close in position to the peaks in the respective experimental PDFs as possible. The initial atomic configurations modified in this way were optimized in terms of energy through MD simulations. In the simulations the value of the SC parameter ε_{ij} was systematically varied within the range of values of the currently used SC parameters ε_{ii} for Au and Pd atoms (listed in Table 1), respectively. Note that our strategy was based on the reasonable assumptions that (i) both the strength of interaction, ε_{ij}, and bonding distance, a_{ij}, between the unlike atoms in the NPs modeled should be some average, respectively, of the strength of interactions, ε_{ii}, and bonding distances, a_{ii}, between the like atoms in these NPs and (ii) MD models reproducing the respective experimental atomic PDFs in good detail should be lower in energy as compared to MD models that do not reproduce the respective experimental atomic PDFs well.

The procedure was iterated and a sizable set of "trial" MD models for each of the Au–Pd alloy NPs was generated. As an example, the energy of the set of "trial" MD models for $Au_{42}Pd_{58}$ alloy NPs is given in Fig. 5.

As can be seen in the figure, and as can be expected, the energy of MD optimized models for $Au_{42}Pd_{58}$ alloy NPs varies with the values of SC parameters a_{ii} and ε_{ii} used. It turned out that the strength of interaction between Au and Pd atoms (i.e. the SC parameter ε_{ij}) in the MD model of lowest energy appeared pretty close to a harmonic average $\left(\varepsilon_{ij} = \dfrac{2\varepsilon_{ii}\varepsilon_{jj}}{\varepsilon_{ii} + \varepsilon_{jj}}\right)$ of the strength of Au–Au and Pd–Pd interactions given in Table 1. The bonding distance between Au and Pd atoms in this model (i.e. the SC parameter a_{ij}) also appeared pretty close to a harmonic average $\left(a_{ij} = \dfrac{2a_{ii}a_{jj}}{a_{ii} + a_{jj}}\right)$ of the Au–Au and Pd–Pd bonding distances given in Table 1. The superiority of the MD model for $Au_{42}Pd_{58}$ alloy NPs based on SC parameters a_{ii} for Au and Pd atoms "re-scaled" as described above and SC parameters a_{ij} and ε_{ij} derived as a harmonic average of the currently used SC parameters a_{ii} and ε_{ii} for Au and Pd over MD models based on the currently used SC parameters a_{ii} for Au and Pd (given in Table 1) and SC parameters a_{ij} and ε_{ij} derived as an arithmetic or geometric average (see eqn (3)) of the currently used SC parameters a_{ii} and ε_{ii} for Au and Pd atoms is demonstrated in Fig. S6 and S7.† It turned out that the SC parameters a_{ij} for Au and Pd atoms in the other Au–Pd NPs studied here also had to be "re-scaled" significantly, though to a different extent for the different NPs. The SC parameters a_{ij} and ε_{ij}, used in the modeling of all other Au–Pd NPs studied here also had to be derived as a harmonic average of the currently used SC parameters a_{ii} and ε_{ii} for Au and Pd atoms. The "re-scaled" SC parameters a_{ij} for Au and Pd atoms in the Au–Pd NPs studied here are summarized in Table 2.

As data in Table 2 show, to be accurate, the SC method should take into account that both Au and Pd atoms in the fresh Au–Pd NPs studied here (i) are somewhat compressed as compared to Au and Pd atoms in bulk Au and Pd, respectively, and (ii) largely do not change in size with the relative Au : Pd ratio. The latter is to be expected since charge transfer between Pd and Au atoms, inducing or induced by a change in their size, can take place only at the Au core–Pd shell interface that is the same for all fresh Au–Pd NPs regardless of whether their Pd shell is one (Au : Pd = 70 : 30), two (Au : Pd = 54 : 46) or four (Au : Pd = 42 : 58) atomic layers thick. On the other hand, to be accurate, the SC method should take into account the fact that not only the size of Au and Pd atoms in the fully activated $Au_{100-x}Pd_x$ alloy NPs ($x = 30, 46$ and 58) is very different from that of Au and Pd atoms in bulk Au–Pd alloys (compare data in Tables 1 and 2) but also it changes irregularly with the NP bimetallic composition. The irregularity is best appreciated when data shown in Table 2 are visualized as was done in Fig. 4B. As can be seen in the figure, changes in the size of Au and Pd atoms in the fully activated Au–Pd alloy NPs with the NP bimetallic composition "mirror" each other, reflecting the complementary behavior of Au and Pd atoms when alloyed at the nanoscale, as discussed above. Furthermore, the SC method should take into account the increased strength of the interactions between Au and Pd atoms in Au–Pd alloy NPs and derive it as a harmonic average of Au–Au and Pd–Pd interactions. Note that the other SC parameters for Au and Pd atoms listed in Table 1, including m_{ii}, n_{ii}, ε_{ii}, and c_i parameters, need not be modified significantly.

Atomic-level models for fresh and fully activated $Au_{100-x}Pd_x$ NPs ($x = 30, 46, 58$) generated by MD simulations based on the SC method/parameters "tuned-up" as described above are shown in Fig. S8† and 6 (left), respectively. The models reproduce the respective experimental PDFs much better than those based on the SC method/parameters currently in use as the comparison between data shown in Fig. 3 and 7 indicate. As such, undoubtedly, the former models are much more relevant to the fresh and fully activated for catalytic applications Au–Pd NPs studied here than the latter ones. However, though of largely improved accuracy, MD models of Fig. 6 (left) fail to reproduce well the respective experimental PDFs at higher r values, in particular the fast decay of the PDFs to zero with increasing r-values (see Fig. 7). Analysis of the models showed that it was the virtual lack of atomic positional disorder near the model's surface (see the nearly uniform facets of the MD models in Fig. 6 (left)) that was behind the failure. Indeed such a failure is to be expected since MD treats all surface

Fig. 5 Energy, E_{tot}, of the set of "trial" models for fully activated $Au_{42}Pd_{58}$ alloy NPs generated by a series of MD runs performed as described in the text. In particular, in the simulations the value of the SC parameter ε_{ij}, i.e. the strength of the interaction between Au and Pd atoms, and the value of the SC parameter a_{ij}, i.e. the bonding distance between Au and Pd atoms, have been systematically varied within the range of values of the currently used SC parameters ε_{ii} and a_{ii} for Au and Pd atoms (listed in Table 1), respectively. An MD model based on SC parameters ε_{ij} and a_{ij} derived as a harmonic average of the currently used SC parameters ε_{ij} and a_{ij} for Au and Pd atoms, respectively, appears of lowest energy (−3.96 eV per atom) as compared to all other MD models tried. For reference, the binding energy of bulk Au is −3.81 eV per atom and that of bulk Pd is −3.89 eV per atom.

Table 2 SC parameters a_{ii} for Au and Pd atoms "tuned up" as described in the text. For convenience, the respective size[a] of Au and Pd atoms is also presented

Model's chemistry	Fresh (core–shell) NPs		Fully activated (alloy) NPs	
	a_{ii} for Au	a_{ii} for Pd	a_{ii} for Au	a_{ii} for Pd
Pure Au seeds	4.044 Å		4.044 Å	
$Au_{70}Pd_{30}$	4.044 Å	3.867 Å	4.044 Å	3.895 Å
$Au_{54}Pd_{46}$	4.044 Å	3.867 Å	3.924 Å	3.910 Å
$Au_{42}Pd_{58}$	4.044 Å	3.867 Å	4.022 Å	3.896 Å
Model's chemistry	Fresh (core–shell) NPs		Fully activated (alloy) NPs	
	Size of Au	Size of Pd	Size of Au	Size of Pd
Pure Au seeds	2.86 Å		2.86 Å	
$Au_{70}Pd_{30}$	2.86 Å	2.74 Å	2.86 Å	2.76 Å
$Au_{54}Pd_{46}$	2.86 Å	2.74 Å	2.78 Å	2.77 Å
$Au_{42}Pd_{58}$	2.86 Å	2.74 Å	2.85 Å	2.76 Å

[a] Atomic size = the respective SC parameter $a_{ij}/\sqrt{2}$.

atoms in metallic NPs alike whereas atoms at the surface of real-world metallic NPs are definitely not alike, at least with respect to the magnitude of positional disorder they can suffer. However, accounting for the usually substantial structural disorder in real-world metallic NPs is important since it can affect their functional properties very substantially.[48] In particular, accounting for the near-surface structural disorder in metallic NPs pursued for catalytic applications is important since it is the NP surface where catalytic reactions take place. Hence, the MD models for fully activated for catalytic applications $Au_{100-x}Pd_x$ alloy NPs (x = 30, 46, 58) shown in Fig. 6 (left) were refined further by hybrid reverse Monte Carlo (RMC) simulations guided by the experimental PDFs. Details of hybrid RMC simulations are given in the ESI.† The RMC-refined structure models are shown in Fig. 6 (right). The respective atomic PDFs reproduce the experimental PDF data very well (see Fig. 7 and the goodness-of-fit indicators, R_{wp}, reported therein), including the region of higher r-values which, as discussed above, is sensitive to the actual degree of atomic positional disorder near the NP surface. Indeed, a closer look at the RMC-refined models (see Fig. 6, bottom) reveals that, in full accord with HR-TEM data of Fig. S2,† their surface is fairly uneven and so more realistic.

The near-surface structural disorder in metallic NPs can also be accounted for analytically, i.e. without invoking a complementary technique for 3D structure simulations such as hybrid RMC. Such an approach may prove very useful in theoretical predictions of metallic NPs, as data in Fig. 11 introduced later on show. Here we demonstrate how it can be done by employing an empirical function first suggested and successfully used by Yevick et al.[73] The function is defined as follows:

$$f(r) = 1 - A + (1 - A)\exp^{(Cr)}, \qquad (4)$$

where $C = \dfrac{1}{R}\ln\left(\dfrac{B-A}{1-A}\right)$, R is the radius of a NP model built/optimized in terms of energy, for example, through MD simu-

lations, r is the distance of atoms in the model from the model's center, and A and B are adjustable parameters. The former sets the rate of increase of the atomic positional disorder with increasing r and the latter accounts for the usual strengthening of that disorder near the NP surface. The approach was tested on the MD models for Au seeds and $Au_{54}Pd_{46}$ alloy NPs shown in Fig. 6 (left) as follows: first, as suggested in ref. 73, the initial values of parameters A and B were set to 1.0 and 0.95, respectively. The value of $f(r)$ for each atom in the MD models was then calculated. Next, random in direction and not larger than 0.02 Å in magnitude displacements for each atom in the models were generated. The magnitude of the displacements was multiplied by the value of $f(r)$ for the respective atoms. The resulting random-type atomic displacements were introduced in the MD models, rendering them more disordered structurally. Atomic PDFs were derived from the models and compared with the respective experimental ones and the misfit between the model-derived and experimental data was evaluated. The values of parameters A and B and the magnitude of random atomic displacement, i.e. the degree of atomic positional disorder in the MD models, were refined until that misfit diminished as much as possible, in particular at higher-r values. The test proved rather successful as data in Fig. S9† show.

Here we also demonstrate that the SC method currently in use needs to be "tuned up" not only in the modeling of less than 10 nm in size binary metal particles but also in the modeling of substantially larger in size monometallic NPs such as 15 nm in size pure Au NPs synthesized and dispersed in water for the purposes of bio-medical applications. Experimental atomic PDFs for the Au NPs, derived from the XRD data of Fig. 3 in ref. 41, and for the polycrystalline Au standard are shown in Fig. 8a (left). As can be seen in the figure and as can be expected, the atomic PDF for polycrystalline Au shows distinct peaks to very high interatomic distances, reflecting the presence of a 3D periodic, long-range order in this essentially bulk (μm-sized) material. On the other hand, peaks in the
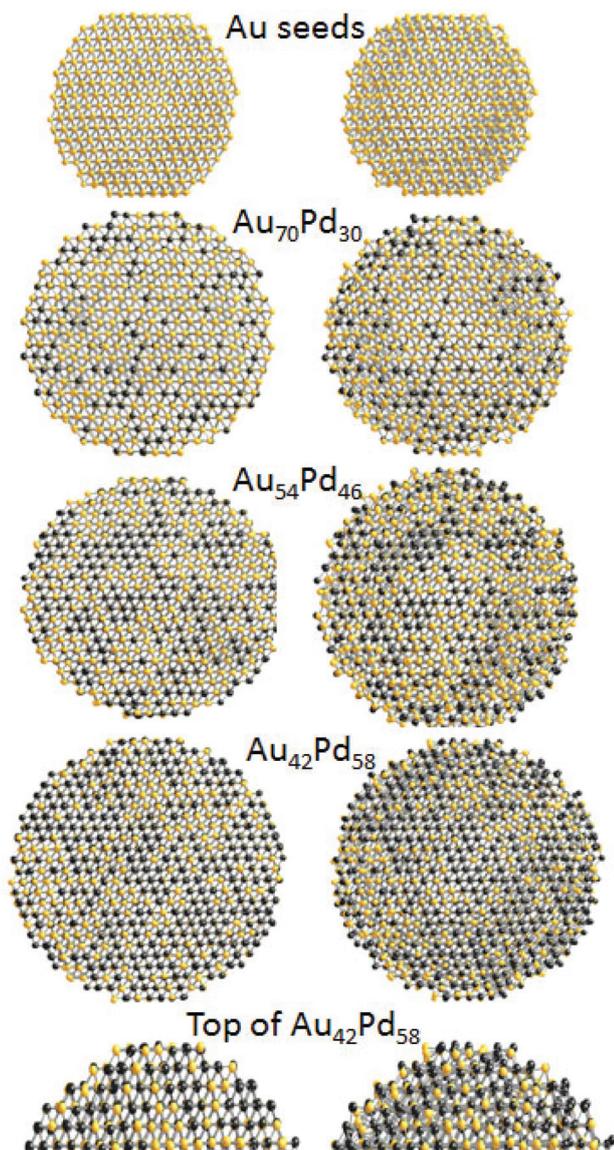
Fig. 6 (Left) 3D structural models for Au seeds and fully activated Au$_{100-x}$Pd$_x$ alloy NPs (x = 30, 46, 58) built by MD simulations based on the SC method/parameters "tuned up" against experimental PDF data as described in the text. The models feature random alloy NPs wherein Au and Pd atoms are fcc-like arranged locally. (Right) Hybrid RMC refined versions of the MD models shown on the left. Corresponding segments of the surface of the MD built and hybrid RMC further refined model for Au$_{42}$Pd$_{58}$ NPs are also shown (at the very bottom) to make clearer the virtual absence and very presence of near-surface structural disorder in the former and latter models, respectively. Au atoms are in yellow and Pd atoms are in black.

Fig. 7 Experimental (black symbols) and MD (blue lines) model-derived atomic PDFs for Au seeds, fresh (Au core–Pd layer) and fully activated (alloy-type) Au$_{100-x}$Pd$_x$ NPs (x = 30, 46 and 58). The respective MD models are shown in Fig. 6 (left). Atomic PDFs derived from the hybrid RMC further refined versions (see Fig. 6, right) of MD models are also shown (red lines). The model's goodness-of-fit indicators, R_{wp}, explained in the ESI,† are shown by each data set in color pertaining to the respective model-derived PDF. The MD models produce atomic PDFs that match the respective experimental data quite well, except for the region of higher-r values. The experimental data are reproduced best by the hybrid RMC further refined models, as a visual inspection and the values of respective R_{wp} indicators are shown.

atomic PDF for the 15 nm Au particles decay to zero at distances (~5 nm) shorter than the particles' physical size as determined by TEM (see Fig. S1, right†). The observed decay indicates that atoms in the 15 nm Au particles suffer substantial atomic positional disorder. The presence of such disorder is revealed clearly when the first peak in the experimental PDF for the Au NPs is compared to that in the experimental PDF

for the polycrystalline Au standard (see the insert in Fig. 8a). The former is considerably broader than the latter, proving the presence of significant structural disorder in the 15 nm Au particles studied here. As may be expected, the degree of structural disorder in the 15 nm Au particles is less than the degree of disorder in the approximately 4 nm in size Au seeds (compare data in the insets of Fig. 3 and 8a). Furthermore, as data in the inset of Fig. 8 (left) show, the first peak in the experimental atomic PDF for the 15 nm in size Au particles is shifted to lower r-values (2.87 Å) as compared to the position of the first peak (2.88 Å) in the PDF for the polycrystalline Au standard. The shift indicates that the Au–Au metal bond length in the NPs is shorter than that in the respective solid by about 0.4%. This may not come as a surprise since experimental studies have shown that the Au–Au metal bond lengths
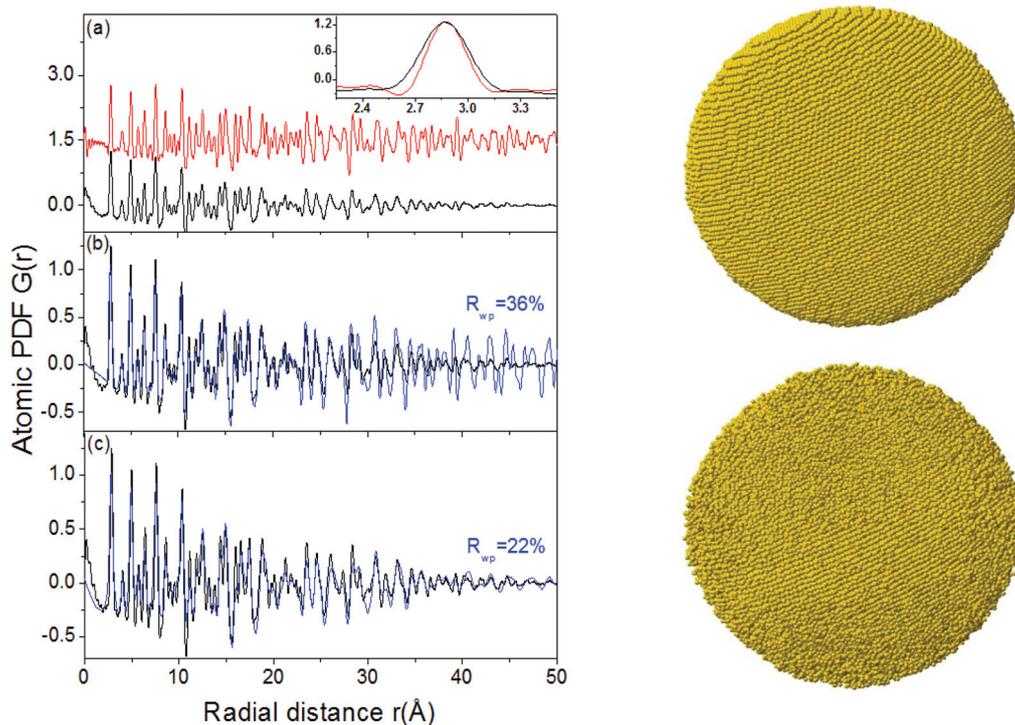
Fig. 8 (Left) (a) Experimental atomic PDFs for 15 nm Au particles (black line) and polycrystalline (bulk) Au standard (red line). The first peaks in the respective PDFs are shown in the inset. The first peak in the PDF for the Au NPs is considerably broader than that in the PDF for bulk Au revealing the presence of extra structural disorder in the former as compared to that (Debye−Waller type) in the latter. Furthermore, the first peak in the atomic PDF for the Au NPs is shifted to lower r-values (2.87 Å) as compared to the position of the first peak in (2.88 Å) in the PDF for bulk Au indicating that the Au−Au metal bond in the NPs is shorter than the Au−Au metal bond in bulk Au. (b) Experimental (black line) and MD model-derived (blue line) atomic PDFs for 15 nm Au particles. The MD model is shown on the right (top). (c) Experimental (black line) and MD model-derived (blue line) atomic PDFs for 15 nm Au particles. The MD model is shown on the right (bottom). Goodness-of-fit indicators, R_{wp}, explained in the ESI,† for the respective models are shown in (b) and (c). (Right top) 3D model for 15 nm Au particles built by MD based on the SC method "tuned up" as described in the text. (Right bottom) A structurally more disordered version of the MD model. The extra structural disorder has been introduced by an empirical procedure explained in the text (see eqn (4)). Models comprise about 105 000 Au atoms.

in Au particles even as large as 50 nm in size can be compressed by about 0.5%. The compression of the Au−Au metal bond length in smaller size (~3–4 nm) Au particles can be as much as 6% as the same studies show.[56]

An atomic-level model for the 15 nm Au particles was built by MD simulations based on the SC method/parameters currently in use (see Table 1). The initial atomic configuration featured a 15 nm in size piece of a fcc-lattice composed of about 105 000 atoms. In optimizing this configuration in terms of energy through MD simulations, the value of the SC parameter a_{ii} for Au had to be reduced from 4.080 Å to 4.060 Å so that the observed 0.4% compression of the Au−Au metal bond in the NPs is accounted for. The optimized MD model, shown in Fig. 8 (top right), reproduces the experimental PDF data quite well at low-r values. However, it fails to reproduce the experimental data at higher-r values (see Fig. 8b, left). As discussed above, such a failure is largely due to the fact that theoretical modeling alone may not account for the actual degree of atomic positional disorder in real-world metallic NPs.

The actual degree of atomic positional disorder in the Au NPs studied here was accounted for by applying the analytical

procedure described above. The resulting structurally more disordered but more realistic model for the Au NPs is shown in Fig. 8 (bottom right).

Here it is worth noting that the MD model shown in Fig. 8 (top right) and its much more disordered version shown in Fig. 8 (bottom right) ended up to be of virtually the same energy of −3.69 eV per atom and −3.68 eV per atom, respectively. For reference, the binding energy of bulk Au is −3.81 eV per atom.[74] This did not come as a surprise since prior studies on approximately 1.5 in size Au particles had found that a DFT-predicted model of the NPs, that did not reproduce the respective experimental PDF data well, and a much more disordered structurally RMC-derived model of the NPs, that reproduced the experimental PDF data very well, appeared to be of virtually the same energy of −2.86 eV per atom and −2.82 eV per atom, respectively.[75] The present and prior findings indicate that, indeed, metallic NPs exhibiting a strong atomic positional disorder are not necessarily less stable than structurally more ordered ones. As our results and studies of others[76] show, it is the size of metallic NPs (e.g. binding energy of −2.86 eV per atom vs. −3.68 eV per atom for 1.5 nm and 15 nm

in size Au NPs, respectively) and not the degree of structural disorder in metallic NPs that affects their stability most. Nevertheless, a metal-to-metal atom bond length compression, even as small as 0.4% as observed with the Au NPs studied here, and the presence of a substantial near-surface structural disorder in metallic NPs should not be neglected since both have been shown to affect their functionality, in particular in biomedical and catalysis-related applications, very substantially.[77,78] An example drawn from such studies[78] is shown in Fig. S10.†

Furthermore, here we demonstrate that the SC method currently in use needs to be "tuned up" not only in the modeling of metallic NPs of the noble metal family, such as Au–Pd and pure Au NPs, but also in the modeling of metallic NPs composed of transition metals, such as $Fe_{48}Pd_{52}$ alloy NPs explored for high-density magnetic recording applications. The applications pursued require that the Fe–Pd NPs are as small as possible in size and exhibit as strong as possible magnetic moment and magnetic anisotropy.[45,79–81] The requirements can be met when Fe and Pd atoms in the NPs are preferentially arranged with respect to each other forming a chemically

ordered nanoalloy. In the nanoalloy Fe atoms would have four Fe and eight Pd first neighbors and the Fe–Pd bonding distances would be shorter than the Fe–Fe and Pd–Pd ones.[82–84]

An experimental atomic PDF for 16 nm in size $Fe_{48}Pd_{52}$ alloy NPs as-synthesized and stored in hexane (see the Experimental section) is shown in Fig. 9a (left). The PDF is extracted from the synchrotron XRD data shown in Fig. 1 in ref. 46. The PDF decays fast with interatomic distances indicating that the $Fe_{48}Pd_{52}$ alloy NPs studied here exhibit substantial structural disorder. First, in the manner described above, the experimental PDF data were approached with simplistic models based on the well-known crystal structures of chemically disordered and ordered bulk $Fe_{50}Pd_{50}$ alloys. The former is of fcc-type (S.G. $Fm\bar{3}m$) with a fcc-lattice parameter $a = 3.88$ Å.[85,86] The latter is of tetragonal-type (S.G. $P4/mmm$) with tetragonal-lattice parameters $a = 3.86$ Å and $c = 3.74$ Å.[85–87] The results of the modeling are shown in Fig. 9a (left). As can be seen in the figure both models reproduce the experimental data relatively well making it virtually impossible to reveal the actual degree of chemical ordering in the $Fe_{48}Pd_{52}$ alloy NPs. Therefore, a more advanced atomic-level model of the NPs was built by MD
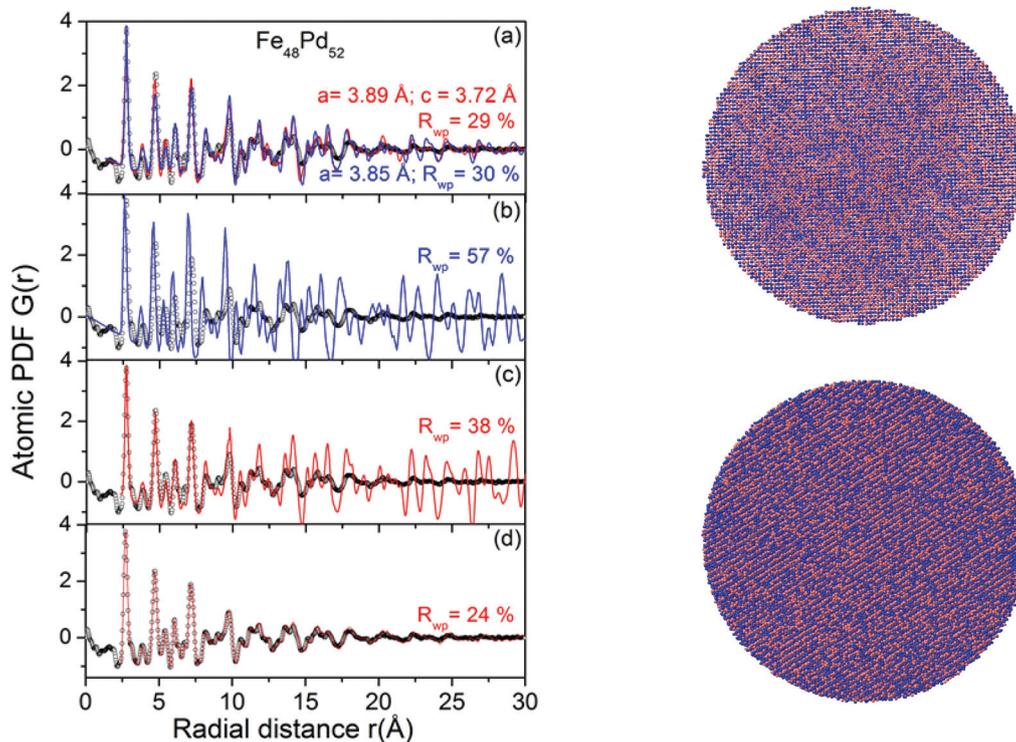
Fig. 9 (Left) Experimental (black symbols) and computed (blue and red lines) PDFs for $Fe_{48}Pd_{52}$ alloy NPs. The computed PDFs in (a) are based on the fcc- (red line) and tetragonal- (blue line) type crystal structures exhibited by chemically disordered and ordered bulk $Fe_{100−x}Pd_x$ alloys ($x \sim 50$), respectively. Values of the NP "fcc- and tetragonal-lattice parameters", derived by adjusting the structure models against the experimental PDF data, are also given. The computed PDF in (b) is derived from a MD model based on the SC method currently in use (see Table 3). The computed PDF in (c) is derived from a MD model based on the SC method "tuned up" as described in the text. The computed PDF in (d) is derived from a hybrid RMC refined version of the "tuned-up" MD model. Goodness-of-fit indicators, R_{wp}, explained in the ESI,† are shown by each data set in color pertaining to the respective model. (Right top) Structural model for $Fe_{48}Pd_{52}$ alloy NPs optimized in terms of energy by MD based on the SC method "tuned up" as described in the text. (Right bottom) A hybrid RMC refined version of the MD model. The models comprise 76 495 Fe (brown) and 82 870 Pd (blue) (in total 159 365) atoms.

Table 3 Currently used SC parameters for densely packed Pd and Fe atoms. The size of Pd and Fe atoms given in the table reflects the value of the SC parameters a_{ii} for Pd and Fe atoms, respectively. Note: the SC parameters for Pd atoms are identical to those listed in Table 1

Metal	m_{ii}	n_{ii}	ε_{ii} (meV)	a_{ii} (Å)	c_i	Size$_{ij}$ (Å)
Pd	6	12	3.2864	3.891	148.2	2.75
Fe	4	15	0.60	3.647	1104.7	2.57

based on the SC method currently in use, including deriving the interactions between unlike atoms as a geometric average of the interactions between like atoms (see eqn (3)). The currently used SC parameters for densely packed Fe and Pd atoms, taken from literature sources,[22,24,88] are listed in Table 3. The initial model featured a 16 nm in size and spherical in shape atomic configuration with the stoichiometry of $Fe_{48}Pd_{52}$ NPs. The optimized in terms of energy model, however, produced an atomic PDF markedly inconsistent with the experimental one as shown in Fig. 9b (left). The result showed clearly that the SC method currently in use needed a "tune-up" for the atomic-level model it produces in order to be relevant to the actual $Fe_{48}Pd_{52}$ alloy NPs studied here. Accordingly, the currently used SC parameters for Fe and Pd were "tuned up" following the approach used in "tuning up" the SC parameters for Au and Pd atoms in Au–Pd NPs described above. It turned out that (i) the values of SC parameters a_{ii} for Fe and Pd atoms had to be modified from 3.647 Å and 3.891 Å (see Table 3) to 3.719 Å and 3.967 Å, respectively, and (ii) the Fe–Pd interactions had to be derived as a harmonic and not as a geometry average of the Fe–Fe and Pd–Pd interactions listed in Table 3. The SC parameters m_{ii}, n_{ii}, ε_{ii}, and c_i for Fe and Pd atoms, listed in Table 3, need not be modified significantly. A model optimized in terms of energy by MD based on the "tuned-up" SC is shown in Fig. 9 (top, right). It reproduces the experimental PDF data quite well, except in the region of higher-r values (see Fig. 9c, left). Note that not only the MD models based on the SC method deriving the interactions between unlike atoms as a geometric or arithmetic average of the interactions between like atoms did not reproduce the experimental PDF data well (see Fig. S11†) but also both turned out to be higher in energy, that was −4.18 eV per atom and −4.45 eV per atom, respectively, as compared to the MD model based on the "tuned-up" SC method (−4.71 eV per atom). As such, undoubtedly, the latter is much more relevant to the $Fe_{48}Pd_{52}$ alloy NPs studied here than the former. The latter model, however, still needed to be imported further since it did not reproduce well the experimental PDF data in the region of higher-r values (see Fig. 9c, left). As discussed above, that region is sensitive to the near-surface structural disorder in metallic NPs.

To account for the actual degree of atomic positional disorder in the $Fe_{48}Pd_{52}$ alloy NPs more precisely, the MD model of Fig. 9 (top, right) was refined further by the hybrid RMC described in the ESI.† The RMC-refined model is shown in Fig. 9 (bottom, right). It reproduces the experimental PDF data very well, including the region of higher-r values as data in

Fig. 9d (left) show. The model was analyzed in terms of the first atomic coordination numbers (CNs). The analysis showed that Fe atoms deep inside the $Fe_{48}Pd_{52}$ alloy NPs have about 4.4(1) Fe and 7.6(1) Pd first neighbors whereas those near the NP surface have about 4.8(1) Fe and 6.8(1) Pd first neighbors. The values of CNs indicated that (i) largely, Fe and Pd atoms in the $Fe_{48}Pd_{52}$ alloy NPs are preferentially arranged with respect to each other and (ii) the degree of this preferential arrangement, $i.e.$ the degree of chemical ordering, somewhat decreases near the NP surface. The model was also analyzed in terms of the first atomic neighbor distances. The analysis showed that the Fe–Pd bond length, as estimated from the position of the first peak in the Fe–Pd partial atomic PDF shown in Fig. S12,† is shorter than the Fe–Fe and Pd–Pd ones, thus corroborating the chemically ordered nature of the $Fe_{48}Pd_{52}$ alloy NPs studied here. Overall, the results of the MD modeling based on the "tuned-up SC" method indicated that the $Fe_{48}Pd_{52}$ alloy NPs exhibit a substantial degree of chemical ordering rendering them suitable for high-density magnetic recording applications.

An important point deserves underscoring here: it is well known that the interdiffusion of atoms in metallic NPs can be several orders of magnitude faster than that of atoms in the respective bulk metals and alloys. As a result, contrary to the case of bulk metals and alloys, atoms in metallic NPs can seek and form energetically favorable configurations at rather moderate, including room, temperature.[13,89,90] Considering this fact and that 3D structure models of energy lower than that of competing models reproduced the experimental PDFs for monometallic Au, random alloy-type $Au_{100-x}Pd_x$ (x = 30, 46, 58) and chemically ordered alloy-type $Fe_{48}Pd_{52}$ NPs best, it may be conjectured that these NPs have attained a rather stable, $i.e.$ native, and not some exotic, vastly transient atomic-level structure. The Au core–Pd shell NPs studied here may also be considered fairly stable at room temperature since they transformed irreversibly into Au–Pd alloy NPs only after a prolonged thermal treatment at 700 K.

With both native and accurate atomic-level models at hand all structural characteristics of the metallic NPs studied can be derived and used to rationalize their properties targeted for optimization. As an example we consider fully activated for catalytic applications $Au_{100-x}Pd_x$ alloy NPs (x = 30, 46 and 58). Distribution of the first Pd–Pd and total ($e.g.$ Pd–Pd + Pd–Ni) CNs for atoms at the NP surface, as derived from the RMC-refined structure models of Fig. 6 (right), is shown in Fig. 10. Note that the Pd–Pd CNs are particularly important for efforts aimed at resolving the yet unsettled debate concerning the
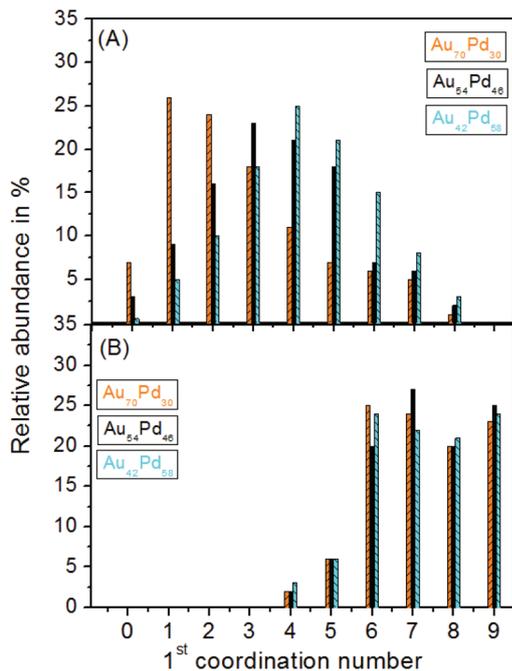
Fig. 10 Distribution of the first (A) Pd–Pd and (B) total coordination numbers for atoms at the surface of fully activated $Au_{100-x}Pd_x$ ($x = 30$, 46, 58) NPs as extracted from their 3D models shown in Fig. 6, right.

contribution of Pd monomers, dimers and tri-clusters to the enhanced catalytic activity of Au–Pd alloy NPs for certain chemical reactions.[31–34,37–39] As can be seen in the figure, the distribution of total CNs appears rather broad reflecting the uneven surface of fully activated Au–Pd NPs. In particular, it shows a large number of 9- and 8-fold coordinated atoms, indicative of close packed, island-type atomic configurations, a substantial number of 7- and 6-fold coordinated atoms, indicative of terraces and edges, and a small but non-negligible number of 5-fold coordinated atoms, indicative of somewhat sharp corners at the NP surface. Also, data in Fig. 10 indicate that the total CNs and, hence, the roughness of the NP surface evolve rather irregularly with the NP bimetallic composition. For example, the number of 6- and 8-fold coordinated atoms in the $Au_{54}Pd_{46}$ NPs appears minimized and that of 7- and 9-fold coordinated ones maximized when compared to the respective CNs for the $Au_{70}Pd_{30}$ and $Au_{42}Pd_{58}$ alloy NPs. The distribution of the first Pd–Pd CNs is also very informative. It reveals that the surface Pd atoms in the fully activated $Au_{100-x}Pd_x$ alloy NPs ($x = 30$, 46 and 58) studied here do not segregate in extended islands and so always have nearby unlike, i.e. Au, atoms to interact/exchange charge with. The distribution of the first Pd–Pd CNs also reveals that the geometry of the atomic configurations made of surface Pd atoms alone changes irregularly with the NP bimetallic composition. For example, about 50% of surface Pd atoms in the $Au_{70}Pd_{30}$ NPs form dimers and tri-clusters whereas the number of surface Pd atoms in the $Au_{54}Pd_{46}$ and $Au_{42}Pd_{58}$ NPs forming such configurations is, respectively, only about 23% and 15%.

An irregular evolution of the configurations of surface Pd atoms and the roughness of the NP surface, known as a geometric effect, and of the intimately coupled length and strength of Au–Pd bonds (see Fig. 4B), known as a ligand effect, is very likely to render the catalytic activity of Au–Pd alloy NPs also evolve irregularly with the NP bimetallic composition.[17] An example of the evolution of the catalytic activity of Au–Pd alloy NPs tracking the irregular evolution of the NP structural features listed above is shown in Fig. 4C. The catalytic activity of Au–Pd alloy NPs for ethylene glycol electro-oxidation and hydrodesulfurization of petroleum feed stock reactions has been found to evolve in a very similar manner.[31–34,64,72] Other, somewhat more sudden fluctuations in the catalytic activity of Au–Pd alloy NPs with the NP bimetallic composition have also been observed.[64,72,91,92] The origin of all these irregularities has remained poorly understood so far. The results presented here can prove invaluable to future studies aiming at unveiling this. Here it may be added that accurate atomic-level modeling of metallic NPs not only can help rationalize their properties targeted for optimization but also provide a sound structural basis for subsequent first principles studies on these properties. In particular, in a recent study on 1.2, 3.4, 3.7 and 5.2 nm in size Ru particles pursued as catalysts for the technologically very important Fischer–Tropsch reaction, realistic 3D models for the NPs have been built and RMC refined. Two atomic layer thick slabs (~150 atoms each) excised from the model's top surface have been optimized further by DFT. The energy barriers for CO dissociation at particular atomic sites on the fragments have been computed and the observed dependence of the rate of the Fischer–Tropsch reaction on the size of Ru NPs has been explained.[93]

Indeed theoretical modeling "tuned up" against experimental atomic PDF data for a few members of a system of metallic NPs not only can describe accurately the particular NPs studied but also predict any other member of that system at the atomic level. As an example an atomic-level model for fully activated for catalytic applications $Au_{88}Pd_{12}$ alloy NPs was built by MD based on the SC method "tuned up" against the experimental PDFs of fully activated $Au_{100-x}Pd_x$ alloy NPs ($x = 30$, 46, 58) as described above. In particular, (i) the SC parameters a_{ii} for Au and Pd atoms in $Au_{88}Pd_{12}$ alloy NPs were derived from the projected evolution of the size of Au and Pd atoms in $Au_{100-x}Pd_x$ alloy NPs ($x = 30$, 46 and 58) with the NP bimetallic composition shown in Fig. 4B (see the respective, "mirroring" each other broken lines) and (ii) the interactions between the unlike atoms in $Au_{88}Pd_{12}$ alloy NPs, i.e. Au–Pd interactions, were derived as a harmonic average of the interactions between like atoms, i.e. as a harmonic average of Au–Au and Pd–Pd interactions. The model is shown in Fig. 11 (top left). It was disordered structurally further, and so made it more realistic to analytically use the empirical procedure based on eqn (4). The values of parameters A and B used in the procedure were set equal to those reported in Fig. S9† so that the degree of structural disorder in $Au_{88}Pd_{12}$ alloy NPs resembles that in $Au_{100-x}Pd_x$ alloy NPs ($x = 30$, 46, 58). The model for $Au_{88}Pd_{12}$ alloy NPs disordered further in this way is shown in Fig. 11
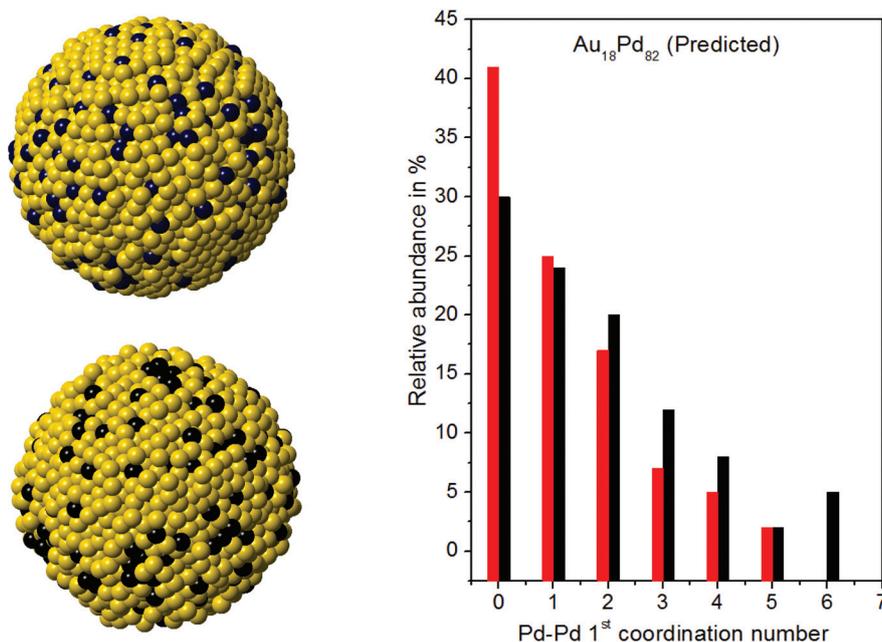
Fig. 11 (Left) (top) Predicted 3D atomic structure of fully activated for catalytic applications $Au_{88}Pd_{12}$ alloy NPs. (bottom) A further disordered structurally and so more realistic version of the predicted 3D structure. Disorder has been introduced using an empirical procedure described in the text (see eqn (4)). (Right) Distribution of surface Pd–Pd CNs in as-predicted (vertical bars in black) and further disordered structurally (vertical bars in red) 3D models for $Au_{88}Pd_{12}$ alloy NPs.

(bottom left). Note that it was not possible to employ hybrid RMC here since no experimental atomic PDF data for the predicted but never synthesized $Au_{88}Pd_{12}$ alloy NPs were available.

Distributions of the surface Pd–Pd CNs in $Au_{88}Pd_{12}$ alloy NPs (red bars) as estimated from (i) the MD model of Fig. 11 (top left) and (ii) its more realistic, further disordered structurally version of Fig. 11 (bottom left) are shown in Fig. 11 (right). The usefulness of the distributions is that they can help assess the catalytic activity of $Au_{88}Pd_{12}$ alloy NPs for technologically important chemical reactions.[31–37] The results of the assessment can then help decide whether it would be worth it to synthesize and explore $Au_{88}Pd_{12}$ alloy NPs as catalysts for these reactions or not. Also, note that, as data in Fig. 11 (right) show, the atomic positional disorder in metallic NPs can affect substantially some of their structural characteristics deemed important for practical, in this case catalytic, applications. Therefore, when substantial, the inherent to metallic NPs atomic positional disorder, in particular that near the NP surface, ought to be accounted for in the atomic-level theoretical modeling and prediction of metallic NPs. Hybrid RMC and the empirical procedure (see eqn (4)) put forward here illustrate how this can be done with success.

Conclusions

Atomic level theoretical modeling relying on assumptions and parameters drawn from simple systems has long been recognized to be useful yet not accurate enough when applied to real-world materials.[94] As may be expected, and as our study

on three exemplary systems of metallic NPs shows, current theoretical methods for modeling metallic NPs at the atomic level are no exception. The main reason is that, for the most part, the methods have been validated against data for perfectly 3D periodic and long-range ordered bulk metals and alloys. As such, the methods can describe very accurately the inherent to bulk metals and alloys structural features that metallic NPs would certainly show, including, for example, the tendency of metallic species to pack as densely as possible, the tendency of metallic species to always pack in a specific way when on their own (*e.g.* fcc-type packing for Au species both in standalone NPs and in the cores of Au core–Pd shell NPs), and many others.[95–97] However, as we show, the methods cannot describe accurately the inherent to metallic NPs alone structural features such as the NP finite size induced change in metal-to-metal bond lengths, the increased (beyond the usual thermal) atomic positional disorder in metallic NPs, the atypical for the respective alloys change in the strength of interactions and bonding distances between unlike metallic species alloyed at the nanoscale, the unforeseen irregular evolution of major structural characteristics of metallic NPs with their composition, and others. Since the foregoing structural features of metallic NPs are known to affect their functionality substantially, extensive research efforts aiming at improving the latter by modifying the former have been under way for quite some time.[1,2,6,8,48,56,86,91,98] For the efforts to succeed, accurate atomic-level knowledge of the actual metallic NPs studied is needed.

The limited ability of theoretical modeling alone to provide such knowledge has long been recognized and attempted to be corrected for. Attempts based on intuition, however, have

largely proven inconclusive. For example, atomic-level models for Au–Pd alloy NPs have also been built by EAM coupled to Monte Carlo simulations.[99] An artificial spline function has been added to the EAM potential in an attempt to account for the low-electron density environments in metallic NPs. On the other hand, the evolution of the "fcc-lattice parameter" of the NPs modeled with the NP bimetallic composition has been assumed to obey Vegard's law strictly. As a result the models' surface has emerged predominantly populated with Au species at any temperature and Au : Pd relative ratio. Though theoretically possible, such models are of a questionable applicability to the actual Au–Pd alloy NPs studied here since, in good accord with the strongly negative enthalpy of formation of bulk Au–Pd alloys for any Au : Pd relative ratio,[100] our and other experimental studies[39] make it clear that Au–Pd NPs optimized for practical applications by post-synthesis treatment at elevated temperature exhibit alloy- and not Pd core–Au shell type structure.

We show that the accuracy of theoretical methods for modeling metallic NPs at the atomic level can be improved to a level required by practical applications when the methods are supplemented with objective, seemingly basic yet crucial information on the atomic arrangement in the actual metallic NPs studied. Information concerns mostly the length and strength of metal-to-metal bonds and, when necessary, the typically substantial atomic positional disorder in metallic NPs.

We show that such information can be provided by atomic PDFs resulting from total scattering experiments on the metallic NPs studied. The suitability of atomic PDFs is due to the fact that they account properly both for the Bragg-like features and substantial diffuse components of the diffraction patterns of metallic NPs and, hence, reflect truly their molecule–solid duality. Note that as the results of the present and many other studies[9–11,25–28,41,46,51,54,55,60–62,75,93] show, total scattering experiments aimed at atomic PDF analysis can be carried out on as-synthesized and/or post-synthesis treated metallic NPs of any size, shape and chemical composition as deposited on solid supports or dispersed in liquids relevant to the practical application pursued.

Also, using the archetypal SC method as an example, we show how, once obtained, experimental atomic PDFs can be used to "tune up" the parameters of theoretical methods for atomic-level modeling of metallic NPs and so improve the methods' accuracy greatly. We argue that not only the SC but also other widely used theoretical methods[18–23,88,97,99] can be improved in the manner demonstrated here since all of the methods rely on precise experimental information for setting the length and strength of metal-to-metal bonds in the metallic NPs modeled. In particular, the method's parameters pertinent to metal-to-metal bond lengths can be modified, to put it simply, "re-scaled", as the model-derived atomic PDFs line up with the respective experimental ones in terms of peak positions as much as possible. The method's parameters pertinent to the strength of interatomic interactions can be adjusted by a variational approach, such as that exemplified in Fig. 5. The approach is based on a very reasonable assumption that the most likely atomic-level structure of the metallic NPs

modeled is the structure, among all the structures feasible, that has the lowest energy possible, given the atomic pair distances and CNs revealed by the respective experimental atomic PDF data. Finer details of the atomic structure of NPs modeled such as, for example, the substantial structural disorder near the NP surface, can be taken care of by hybrid RMC simulations or the empirical procedure based on eqn (4). It is noteworthy that theoretical modeling of real-world metallic NPs can be made not only more accurate in the manner described above but also more efficient than now. This can be achieved by considering not all theoretically feasible NP structure models but only those that are consistent with the size, shape, phase state, structure type and preparation conditions of the particular NPs modeled using clues provided by complementary experiments (e.g. TEM, HAADF-STEM etc.) and/ or simplistic modeling (e.g. crystal-structure constrained modeling) yet not ignoring ranking of the models considered with respect to their energy, i.e. stability, as was done here. Indeed intentionally reducing the space of possible structure models that need to be searched so as to improve the efficiency of theoretical modeling of metallic NPs at the atomic level has been practiced with success for quite some time.[101,102]

Furthermore, based on examples drawn from the present study, we argue that once "tuned up" against experimental PDF data, theoretical modeling not only can provide a clear 3D picture of the outcome of synthesis and post-synthesis treatment of metallic NPs, as is the case with the $Fe_{48}Pd_{52}$ alloy NPs studied here, but also allow assessing of the structural characteristics of metallic NPs deemed important for achieving the sought after functionality accurately, as is the case with Au–Pd alloy NPs studied here (e.g. see Fig. 11). The latter can help in understanding the synthesis–atomic structure–property relationships in metallic NPs (e.g. see data in Fig. 4B and C). The former can provide a feedback loop for streamlining their synthesis and optimization for practical applications. Another relevant example comes from recent studies on Pt–Ru alloy NPs explored as catalysts for gas-phase CO oxidation and ethanol electro-oxidation reactions. Models built by MD based on the SC method "tuned up" as described here and refined further by hybrid RMC have provided strong evidence that ligand (electronic) and practically unrecognized so far atomic ensemble effects contribute to the remarkable catalytic activity of Pt_xRu_{100-x} alloy NPs with $x \sim 50$ for the aforementioned reactions. The findings have indicated new routes for improving the catalytic activity of Pt–Ru alloy NPs further by enhancing the ligand and atomic ensemble effects the NPs exhibit. Models built by MD based on the SC method currently in use have failed in this regard.[103]

Last but not least, we argue that "tuning up" theoretical modeling by total scattering experiments on a few members of a system of metallic NPs explored for a particular application can unleash theory's predictive power, allowing evaluating the potential of any member of that system for that particular application on a computer and not in the lab, as exemplified in Fig. 11. Ultimately this will help advance nanoscience and technology a step closer to producing metallic NPs by rational design.

Acknowledgements

References

1 B. R. Cuenya, Synthesis and catalytic properties of metal nanoparticles: Size, shape, support, composition, and oxidation state effects, *Thin Solid Films*, 2010, **518**, 3127.

2 G. A. Samorjai, *Introduction to surface chemistry and catalysis*, Wiley, New York, 1994.

3 D. Antoniak, M. Spasova, A. Trunova, K. Fauth, A. R. Wilhelm, J. Minar, H. Ebert, M. Farle and H. Wende, Inhomogenous alloying in FePt nanoparticles as a reason for reduced magnetic moments, *J. Phys. Condens. Matter*, 2009, **21**, 336002.

4 D. Carta, G. Mountjoy, M. Gass, G. Navarra, M. F. Casula and A. Corriasc, Structural characterization study of FeCo alloy nanoparticles in a highly porous aerogel silica matrix, *J. Chem. Phys.*, 2007, **127**, 204705.

5 R. F. L. Evans, R. W. Chantrell and O. Chubykalo-Fesenko, Surface and interface effects in core–shell particles, *MRS Bull.*, 2013, **38**, 909–913.

6 S. Link, Z. L. Wang and M. A. El-Sayed, Alloy Formation of Gold-Silver nanoparticles and the Dependence of the Plasmon Absorption on their composition, *J. Phys. Chem.*, 1999, **103**, 3529–3533.

7 P. Tartaj, M. d. P. Morales, S. Veintemillas-Verdaguer, T. Gonzalez-Carreno and C. J. Serna, The preparation of magnetic nanoparticles for applications in biomedicine, *J. Phys. D: Appl. Phys.*, 2003, **36**, R182–R917.

8 C.-A. J. Lin, C.-H. Lee, J.-T. Hsieh, H. H. Wang, J. K. Li, J. L. Shen, W. H. Chan, H.-I. Yeh and W. H. Chang, Synthesis of fluorescent metallic nanoclusters toward biomedical application: recent progress and present challenges, *Jpn. J. Med. Electron. Biol. Eng.*, 2009, **29**, 276–283.

9 T. Egami and S. L. Billinge, *Underneath the Bragg peaks: Structural Analysis of Complex Materials*, Pergamon Press, Elsevier Ltd, New York, 2003.

10 V. Petkov, Nanostructure by high-energy XRD, *Mater. Today*, 2008, **11**, 28–38.

11 K. Page, T. C. Hood, T. Proffen and R. B. Neder, Building and refining complete nanoparticle structures with total scattering data, *J. Appl. Crystallogr.*, 2011, **44**, 327–336.

12 W. J. Huang, R. Sun, J. Tao, L. D. Menard, R. G. Nuzzo and J. M. Zuo, Coordination-dependent surface atomic contraction in nanocrystals revealed by coherent diffraction, *Nat. Mater.*, 2008, **7**, 308–313.

13 D. Marks, Experimental studies of small particle structures, *Rep. Prog. Phys.*, 1994, **57**, 603–649.

14 A. Frenkel, Solving the 3D structure of nanoparticles, *Z. Kristallogr.*, 2007, **222**, 605–611.

15 D. Yuan, X. Gong and R. Wu, Peculiar distribution of Pd on Au nanoclusters: First-principles studies, *Phys. Rev. B: Condens. Matter*, 2008, **78**, 035441.

16 F. Vines, J. R. B. Gomes and F. Illas, Understanding the reactivity of metallic nanoparticles: beyond the extended surface model for catalysis, *Chem. Soc. Rev.*, 2014, **43**, 4922–4939.

17 P. Liu and J. K. Norskov, Ligands and Ensemble Effects in Adsorption on Alloy Surfaces, *Phys. Chem. Chem. Phys.*, 2001, **3**, 3814–3818.

18 D. Yuan, X. Gong and R. Wu, Atomic Configurations of Pd atoms in PdAu(111) bimetallic surfaces investigated using the first-principles pseudopotential plane wave approach, *Phys. Rev. B: Condens. Matter*, 2007, **75**, 085428.

19 G. Mazzone, I. Rivalta, N. Russo and S. Emilia, Interactin of CO with PdAu(111) and PdAu(100) bimetallic surfaces: A theoretical cluster model study, *J. Phys. Chem. C*, 2008, **112**, 6073–6081.

20 M. S. Daw and M. I. Baskes, SemiempiricalQuantum Mechanical Calculation of Hydrogen Embrittlement in Metals, *Phys. Rev. Lett.*, 1983, **50**(17), 1285–1288.

21 S. M. Foiles, M. I. Baskes and M. S. Daw, Embedded-atom-method functions for the fcc metals Cu, Ag, Au, Ni, Pd, Pt, and their alloys, *Phys. Rev. B: Condens. Matter*, 1986, **33**, 7983.

22 M. W. Finnis and J. E. Sinclair, A simple empirical N-body potential for transition metals, *Philos. Mag. A*, 1984, **50**, 45–55.

23 F. Erocolessi, E. Tosatti and M. Parinello, Au(100) Surface Reconstruction, *Phys. Rev. Lett.*, 1986, **57**(6), 719.

24 A. P. Sutton and J. Chen, Long-range Finnis–Sinclair potentials, *Philos. Mag. Lett.*, 1990, **61**, 139–146.

25 V. Petkov, S. Shan, P. Chupas, J. Yin, L. Yang, J. Luo and C.-J. Zhong, Noble-transition metal nanoparticle breathing in a reactive gas atmosphere, *Nanoscale*, 2013, **5**, 7379–7387.

26 V. Petkov, Y. Lee, S. Sun and Y. Ren, Noncrystallographic atomic arrangement driven enhancement of the catalytic activity of Au nanoparticles, *J. Phys. Chem. C*, 2012, **116**, 26668–26673.

27 F. L. Deepak, G. Casillas-Garcia, R. Esparza, H. Barron and M. J. Yacaman, New insights into the structure of Pd–Au nanoparticles as revealed by aberration-corrected STEM, *J. Cryst. Growth*, 2011, **325**, 60–67.

28 V. Petkov, R. Loukrakpam, L. Yang, B. N. Wanjala, J. Luo, C.-J. Zhong and S. Shastri, Pt-Au alloying at the nanoscale, *Nano Lett.*, 2012, **12**, 4289.

29 L. Deng, W. Hu, H. Deng and S. Xiao, Surface Segregation and Structural Features of Bimetallic Au–Pt Nanoparticles, *J. Phys. Chem. C*, 2010, **114**(25), 11026–11032.

30 H. Rafii-Tabar and A. S. Sutton, Long-range Finnis–Sinclair potentials for fcc metallic alloys, *Philos. Mag. Lett.*, 1991, **63**, 217.

31 J. Edwards, A. F. Carley, A. A. Herzing, C. J. Kiely and G. J. Hutchings, Direct synthesis of hydrogen peroxide from H_2 and O_2 using supported Au–Pd catalysts, *Faraday Discuss.*, 2008, **138**, 225–239.

32 T. T. David, Catalysis by Gold/Platinum Group Metals, *Platinum Metals Rev.*, 2004, **48**(4), 169–172.

33 J. Xu, T. White, P. Li, C. He, J. Yu, W. Yuan and Y. Han, Biphasic Pd-Au alloy catalysts for low-temperature CO oxidation, *J. Am. Chem. Soc.*, 2010, **132**(30), 10398–10406.

34 P. Miedziak, Q. He, J. Edwards, P. Landon, B. Solsona-Espriu, A. F. Carley, A. Herzing, M. Watanave, C. Kiely, D. Knight and G. Hutchings, Oxidation of benzyl alcohol using supported gold-palladium nanoparticles, *Catal. Today*, 2011, **163**, 47–54.

35 H. Ham, G. S. Hwang, J. Han, S. Nam and T. Lim, Geometric Parameter Effects on ensemble Contributions to Catalysis: H_2O_2 Formation from H_2 and O_2 on AuPd Alloys. A First Principles Study, *J. Phys. Chem. C*, 2010, **114**, 14922–14928.

36 B. Pawelec, A. M. Venezia, V. La Parola, E. Cano-Serrano, J. M. Campos-Martin and J. L. G. Fierro, AuPd Alloy Formation in Au–Pd/Al_2O_3 Catalysts and Its Role on Aromatics Hydrogenation, *Appl. Surf. Sci.*, 2005, **242**, 380–391.

37 A. E. Baber, H. L. Tierney and E. C. Sykes, Atomic-Scale Geometry and Electronic Structure of Catalytically Important Pd/Au Alloys, *ACS Nano*, 2010, **4**, 1637–1645.

38 L. Guczi, A. Beck, A. Horvath, Z. Koppany, G. Stefler, K. Frey, I. Sajo, O. Geszti, D. Bazin and J. Lynch, AuPd bimetallic nanoparticles on TiO_2; XRD, TEM, in situ EXAFS studies and catalytic activity in CO oxidation, *J. Mol. Catal. A: Chem.*, 2003, **204**, 545–552.

39 P. Dash, T. Bond, C. Fowler, W. Hou, N. Coombs and R. W. J. Scott, Rational Design of Supported PdAu Nanoparticle Catalysts from Structured Nanoparticle Precursors, *J. Phys. Chem. C*, 2009, **113**(29), 12719–12730.

40 A. R. Wilson, K. Sun, M. Chi, R. M. White, J. M. LeBeau, H. H. Lamb and B. J. Wiley, From core–shell to alloys: The preparation and characterization of solution-synthesized AuPd nanoparticle catalysts, *J. Phys. Chem. C*, 2013, **117**, 17555–17566.

41 V. Petkov, Y. Peng, G. Williams, B. Huang, D. Tomalia and Y. Ren, Structure of Au nanoparticles in water studied by x-ray diffraction and computer simulations, *Phys. Rev. B: Condens. Matter*, 2005, **72**, 195402.

42 S. Xiangyang, W. Suhe and J. R. Baker, Dendrimer-entrapped gold nanoparticles as a platform for cancer-cell targeting and imaging, *Small*, 2007, **3**, 1245–1252.

43 Li Du, W. Shihui and S. Xiangyang, Dendrimer-entrapped metal colloids as imaging agents, *WIREs Nanomed. Nanobiotechnol.*, 2015, **7**, 678–690.

44 M. K. Calabretta, K. S. Matthews and V. L. Colvin, DNA Binding to Protein-Gold Nanocrystal Conjugates, *Bioconjugate Chem.*, 2006, **17**, 1156–1161.

45 Y. Hou, H. Kondoh, T. Kogure and T. Ohta, Preparation and characterization of monodisperse FePd NPs, *Chem. Mater.*, 2004, **16**, 5149.

46 V. Petkov, T. Ohta, Y. Hou and Y. Ren, Atomic-scale Structure of Nanocrystals by High-Energy X-ray Diffraction and Atomic Pair Distribution Function Analysis: Study of Fe_xPd_{100-x} ($x = 0, 26, 28, 48$) nanoparticles, *J. Phys. Chem. C*, 2007, **111**, 714.

47 V. Petkov, RAD, a program for analysis of X-ray diffraction data from amorphous materials for personal computers, *J. Appl. Crystallogr.*, 1989, **22**, 387.

48 Y. Tang and M. Ouyang, Tailoring properties and functionalities of metallic NPs through crystallinity engineering, *Nat. Mater.*, 2007, **6**, 754.

49 S. O. Kart, M. Tomak, M. Uludogan and T. Cagin, Structural, thermodynamical, and transport properties of undercooled binary Pd-Ni alloys, *Mater. Sci. Eng., A*, 2006, **435–436**, 736–744.

50 W. B. Pearson, *The crystal chemistry and physics of metals and alloys*, Wiley-Interscience, New York, 1972.

51 V. Petkov and S. Shastri, Element-specific structure of materials with intrinsic disorder by high-energy resonant x-ray diffraction and differential atomic pair-distribution functions: A study of PtPd nanosized catalysts, *Phys. Rev. B: Condens. Matter*, 2010, **81**, 165428.

52 L. Farrow, P. Juhas, J. Liu, D. Bryndin, E. Bozin, J. Bloch, T. Proffen and S. Billinge, PDFfit2 and PDFgui: computer programs for studying nanostructure in crystals, *J. Phys.: Condens. Matter*, 2007, **19**, 335219.

53 *X-Ray Diffraction Procedures: For Polycrystalline and Amorphous Materials*, ed. P. K. Klug and L. E. Alexander, Wiley, 1974.

54 M. A. Newton, K. Chapman, D. Thompsett and P. J. Chupas, Chasing changing nanoparticles with time resolved PDFs, *J. Am. Chem. Soc.*, 2012, **134**, 5036.

55 N. Bedford, G. Viau, P. Chupas and V. Petkov, 3D structure of nanosize catalysts by high-energy XRD and RMC simulations: study of Ru, *J. Phys. Chem. C*, 2007, **111**, 18214.

56 T. Miller, A. J. Kropf, Y. Zha, J. R. Regalbuto, L. Dellanoy, C. Louis, E. Bus and J. A. van Brokhoven, The effect of gold particle size on Au–Au bond lengths and reactivity toward oxygen in supported catalysts, *J. Catal.*, 2006, **240**, 222.

57 S. Shan, V. Petkov, L. Yang, J. Luo, P. Joseph, D. Mayzel, B. Prasai, L. Wang, M. Engelhard and C.-J. Zhong, Atomic-structural synergy for catalytic oxidation of CO over Pd–Ni nanoalloys, *J. Am. Chem. Soc.*, 2014, **136**, 7140.

58 S. Shan, V. Petkov, L. Yang, D. Mott, B. N. Wanjala, F. Cai, B. H. Chen, J. Luo and Ch.-J. Zhong, Oxophilicity and Structural Integrity in Maneuvering Surface Oxygenated Species on Nanoalloys for CO Oxidation, *ACS Catal.*, 2013, **13**, 3075.

59 J. Yin, S. Shan, L. Yang, D. Mott, O. Malis, V. Petkov, F. Cai, M. S. Ng, J. Luo, B. H. Chen, M. Engelhard and C. J. Zhong, Gold–Copper Nanoparticles: Nanostructural Evolution and Bifunctional Catalytic Sites, *Chem. Mater.*, 2012, **24**, 4662.

60 V. Petkov, L. Yang, J. Yin, R. Loukrakpam, S. Shan, B. Wanjala, J. Luo, K. W. Chapman and C.-J. Zhong, Reactive Gas Environment Induced Structural Modification of Noble-Transition Metal Nanoparticles, *Phys. Rev. Lett.*, 2012, **109**, 125504.

61 Y. Lei, H. Zhao, R. D. Rivas, S. Lee, B. Liu, J. Lu, E. Stach, R. E. Winans, K. W. Chapman, J. P. Greeley, J. T. Miller, P. J. Chupas and J. W. Elam, Adsorbate-Induced Structural Changes in 1–3 nm Platinum Nanoparticles, *J. Am. Chem. Soc.*, 2014, **136**, 9320.

62 V. Petkov, S. Shastri, S. Shan, P. Joseph, J. Luo, C. J. Zhong, T. Nakamura, Y. Herbani and S. Sato, Resolving Atomic Ordering Differences in Group 11 Nanosized Metals and Binary Alloy Catalysts by Resonant High-Energy X-ray Diffraction and Computer Simulations, *J. Phys. Chem. C*, 2013, **117**, 22131.

63 A. L. Allred, Electronegativity values from thermochemical data, *J. Inorg. Nucl. Chem.*, 1961, **17**(3–4), 215–221.

64 F. Gao and D. A. Goodman, Pd-Au bimetallic catalysts: understanding alloy effects from planar and supported nanoparticles, *Chem. Soc. Rev.*, 2012, **41**, 8009–8020.

65 Y.-S. Lee, Y. Jeon and S.-J. OH, Charge redistribution and electronic behaviour in Pd-Au alloys, *J. Korean Phys. Soc.*, 2000, **37**, 451–455.

66 L. Pauling, Electron transfer in intermetallic compounds, *Proc. Natl. Acad. Sci. U. S. A.*, 1950, **36**, 533.

67 L. Pauling, *The Nature of the Chemical Bond*, Cornell University Press, Ithaca, NY, 1975.

68 L. Pauling, Factors Determining the Average Atomic Volumes in Intermetallic Compounds, *Proc. Natl. Acad. Sci. U. S. A.*, 1987, **84**, 4754–4756.

69 B. W. Pearson, The geometrical factor in the crystal chemistry of metals: near-neighbor diagrams, *Acta Crystallogr., Sect. B: Struct. Sci.*, 1968, **24**, 1415.

70 T. Rajasekharan and V. Seshubai, Charge transfer on the metallic atom-pair bond, and the crystal structures adopted by intermetallic compounds, *Acta Crystallogr., Sect. A: Found. Crystallogr.*, 2012, **68**, 156–165.

71 A. R. Denton and N. W. Ashcroft, Vegard's law, *Phys. Rev. A*, 1991, **43**, 3161–3164.

72 M. Brandalise, M. Tusi, R. M. Piasentin, M. d. Santos, E. Spinace and A. Neto, Synthesis of PdAu/C and PdAuBi/C electrocatalysts for ethylene Glycol electrooxidation in Alkaline medium, *Int. J. Electrochem. Sci.*, 2012, **7**, 9609–9612.

73 A. Yevick and A. I. Frenkel, Effects of surface disorder on EXAFS modeling of metallic clusters, *Phys. Rev. B: Condens. Matter*, 2010, **81**, 115451.

74 K. Charles, *Introduction to Solid State Physics*, John Wiley & Sons, Inc, Hoboken, NJ, 8th edn, 2005.

75 V. Petkov, N. Bedford, M. R. Knecht, M. G. Weir, R. M. Crooks, W. Tang, G. Henkelman and A. Frenkel, Periodicity and atomic ordering in nanosized particles of crystals, *J. Phys. Chem. C*, 2008, **112**, 8907.

76 C. Q. Sun, Size dependence of nanostructures: impact of bond order deficiency, *Prog. Solid State Chem.*, 2007, **35**, 1.

77 H. Hakkinen, The gold sulfur interface at the nanoscale, *Nat. Chem.*, 2012, **4**, 443–455 and references cited therein.

78 N. M. Bedford, H. Ramezani-Dakhel, J. M. Slocik, B. D. Briggs, Y. Ren, A. I. Frenkel, V. Petkov, H. Heinz, R. R. Naik and M. R. Knecht, Elucidation of Peptide-directed Pd Surface Structure for Biologically Tunable Nanocatalysts, *ACS Nano*, 2015, **9**, 52 (Journal Cover Story).

79 F. Domestre, B. Choudret, C. Amiens, P. Renaud and P. Fejes, Superlattices of Fe nanocubes synthesized from Fe N(SiMe$_3$)$_2$, *Science*, 2004, **303**, 821.

80 M. Green and P. O'Brien, The preparation of organically functionalised chromium and nickel nanoparticles, *Chem. Commun.*, 2001, 1912.

81 X. X. Zhang, H. L. Wei, Z. Q. Zhang and L. Zhang, Anisotropic magnetocaloric effect in nanostructured Magnetic cubes, *Phys. Rev. Lett.*, 2001, **87**, 57203.

82 D. E. Laughlin, K. Srinavasan, M. Tanase and L. Wang, Crystallographic aspects of L10 magnetic materials, *Scr. Mater.*, 2005, **55**, 383.

83 K. Watanabe, H. Kura and T. Sato, Transformation to L1o structure in FePd nanoparticles synthesized by modified polyol process, *Sci. Technol. Adv. Mater.*, 2006, **7**, 145.

84 M. Chen and D. E. Nikles, Synthesis of spherical FePd and CoPt nanoparticles, *J. Appl. Phys.*, 2002, **91**, 8477–8479.

85 *Springer Handbook: Condensed Matter and materials Data*, ed. W. Martienssen and H. Warlimont, Springer, Berlin, Heidelberg, 2005, part 3.

86 P. Villars and L. D. Calvert, *Pearson's Handbook of Crystallographic data to Intermetallic phases*, ASM, Metals Park, OH, 2nd edn, 1991.

87 Y. Chen, T. Atago and T. Mohri, First-Principles study for ordering and phase separation in Fe-Pd system, *J. Phys.: Condens. Matter*, 2002, **14**, 1903.

88 T. Shen, W. Meng, Y. Yongquan and X. Lu, Size dependence and phase transitions during melting of fcc-Fe nanoparticles: a MD study, *Appl. Surf. Sci.*, 2013, **227**, 7 and references cited therein.

89 Q. Zhang, J. Yang Lee, J. Yang, Ch. Boothroyd and J. Zhang, Size and composition tunable Ag–Au alloy nanoparticles by replacement reactions, *Nanotechnology*, 2007, **18**, 245605.

90 H. Yasuda and H. Mori, Spontaneous alloying of zinc atoms onto clusters and formation of compound clusters, *Phys. Rev. Lett.*, 1992, **69**, 3747.

91 Y.-F. Han, Z. Zhong, K. Ramesh, F. Chen, L. Chen, T. White, Q. Tay, N. Y. Siti and Z. Wang, Au Promotional Effects on the Synthesis of H$_2$O$_2$ Directly from H$_2$ and O$_2$ on Supported Pd-Au Alloy Catalysts, *J. Phys. Chem. C*, 2007, **111**, 8410–8413.

92 M. Chen, D. Kumar, C.-W. Yi and D. W. Wayne, The Promotional Effect of Gold in Catalysis by Palladium-Gold, *Science*, 2005, **310**(5746), 291–293.

93 X.-Y. Quek, I. A. W. Filot, R. Pestman, R. A. van Santel, V. Petkov and J. M. Hensen, Correlating Fischer–Tropsch activity to Ru NP surface structure as probed by high-energy XRD, *Chem. Commun.*, 2014, **50**, 6005.

94 E. A. Carter, Challenges in Modeling Materials Properties without Experimental Input, *Science*, 2008, **321**, 800–803.

95 R. Ferrando, J. Jellinek and R. L. Johnston, Nanoalloys: From theory to applications of alloy clusters and nanoparticles, *Chem. Rev.*, 2008, **108**, 845–910.

96 B. Hammer and J. K. Norskov, Theoretical surface science and Catalysis – calculations and concepts, *Adv. Catal.*, 2009, **45**, 71.

97 R. Ferrando, Computational Methods for Predicting the Structures of Nanoalloys, in *Nanoalloys Engineering Materials*, 2012, pp. 259–286.

98 E. Antolini, Effect of the structural characteristics of binary Pt-Ru and ternary Pt-Ru-M fuel cell catalysts on the activity of electro-oxidation of ethanol in acid medium, *ChemSusChem*, 2013, **6**, 966.

99 B. Shan, L. Wang, S. Yang, J. Hyun, N. Kapur, Y. Zhao, J. B. Nicholas and K. Cho, First-principles-based embedded atom method for PdAu nanoparticles, *Phys. Rev. B: Condens. Matter*, 2009, **80**, 035404.

100 P. Weinberger, J. Kudrnovsky, J. Redinger, B. Bennett and A. M. Boring, Calculation of equilibrium lattice parameter and the heat of mixing for the system Au/Pd by the relativistic Korringa-Kohn-Rostoker coherent-potential-approximation method, *Phys. Rev. B: Condens. Matter*, 1993, **48**, 7866.

101 D. Bochiccio and R. Ferrado, Morphological instability of core–shell metallic nanoparticles, *Phys. Rev. B: Condens. Matter*, 2013, **87**, 165435.

102 D. J. Wales and J. P. K. Doye, Global Optimization by Basin-Hopping and the Lowest Energy Structures of Lennard-Jones Clusters Containing up to 110 Atoms, *J. Phys. Chem. A*, 1997, **101**, 5111.

103 B. Prasai, Y. Ren, Sh. Shan, Y. Zhao, C. H. Cronk, J. Luo, C.-J. Zhong and V. Petkov, Synthesis-atomic structure-properties relationships in metallic nanoparticles by total scattering experiments and 3D computer simulations: case of Pt-Ru nanoalloy catalysts, *Nanoscale*, 2015, **7**, 8122.